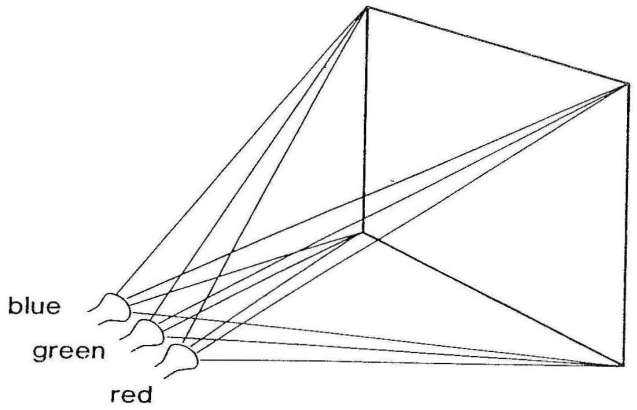

Fig. 7.3. Principle of projection television. The images of three smaller cathode-ray tubes (blue, green and red) are projected to a large screen

There are many other types of cathode-ray tubes which find application: oscilloscope tubes, tubes with very short decay times, radar tubes, tubes with high-resolution screens, and so on. For these tubes and the phosphors they require, we refer to a recent review paper [1].

7.2 Preparation of Cathode-Ray Phosphors

Much of what has been said in Sect. 6.3 on lamp phosphors, can be repeated here. Since fast electrons excite the host lattice and create mobile electrons and holes, the restrictions to the impurity level are usually even more severe. This is certainly the case for the frequently applied sulfides. In principle zinc sulfides are made by dissolving ZnO in sulfuric acid yielding an aqueous solution of $ZnSO_4$. Subsequently H_2S is bubbled through the solution, converting $ZnSO_4$ into insoluble ZnS. The shape, size and crystal quality of this precipitate depends on the reaction conditions (pH, temperature, concentration).

The raw material is then fired with a flux and the activator, and the product is sieved. Finally the flux is removed and the product milled. Suitable processes may be applied to obtain particles of the described size ($\sim 5\ \mu m$).

The red-emitting $Y_2O_2S : Eu^{3+}$ is made from a mixture of the oxides and elemental sulfur which is heated in a flux consisting of sodium carbonate and alkaline phosphate. The fired product is washed with diluted HCl in order to remove Na_2S. Figure 7.4 shows a scanning electron microscope photograph of an oxysulphide phosphor.

Several methods are in use to fabricate the luminescent screen in the cathode-ray tube. For conventional applications the screen thickness is 15–30 μm, i.e. 2–4 particles deep, resulting in a weight of 3–7 mg/cm^2. The setting method has been used since the beginning of tube manufacturing and is still in use for monochrome

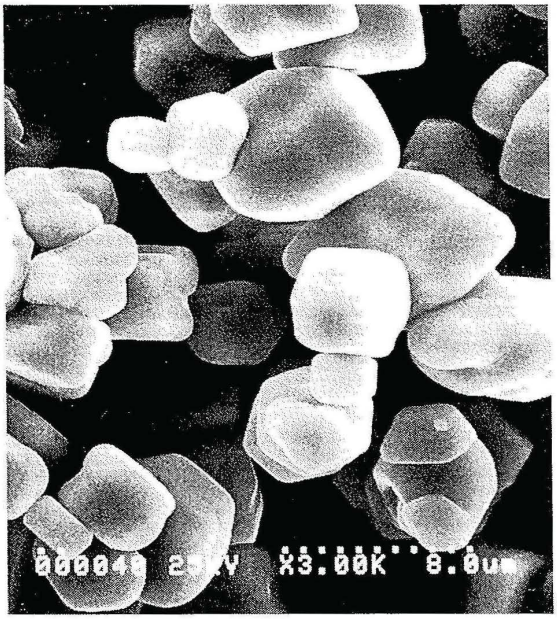

Fig. 7.4. Scanning electron microscope photograph of particles of the $Y_2O_2S:Eu$ phosphor. (reproduced with permission from Ref. [1])

cathode-ray tubes. In order to produce color tubes, predominantly a slurry method is used. Further a dusting and an electrophoretic method can be used. For more details on screening, see Ref. [1].

7.3 Cathode-Ray Phosphors

7.3.1 Some General Remarks

The host lattices which yield the highest radiant efficiency (Sect. 4.3) for cathode-ray excitation are undoubtedly ZnS and its derivatives. For the blue-emitting ZnS : Ag values higher than 20% have been reported. We note that this fits our discussion in Sect. 4.4, where the maximum efficiency for host lattice excitation was found to occur for small values of the band gap E_g and the vibrational frequency ν_{LO} (Eqs (4.5)–(4.7)). For ZnS $E_g = 3.8$ eV and $\nu_{LO} = 350\ cm^{-1}$. These values satisfy our requirements. This can be illustrated by Y_2O_3 with $E_g = 5.6$ eV and $\nu_{LO} = 550\ cm^{-1}$, yielding a maximum efficiency of only 8%. Although the latter value is for red emission, this value is much lower than for ZnS.

It is in principle very simple to change the emission wavelength of the efficient blue cathode-ray phosphor ZnS : Ag^+, viz. by replacing part of the zinc by cadmium.

As a consequence the band gap decreases, so that the emission wavelength shifts to the red. Actually $Zn_{0.68}Cd_{0.32}S:Ag^+$ is a green-, and $Zn_{0.13}Cd_{0.87}S:Ag^+$ a red-emitting cathode-ray phosphor. The emission color is not determined by the nature of the luminescent center, but by the value of the band gap. Figure 7.2 shows the chromaticity diagram with three phosphors from the $(Zn,Cd)S:Ag^+$ family.

However, the (Zn,Cd)S system has several disadvantages. In the first place, the use of cadmium has become inacceptable for environmental reasons. The red phosphor on this basis has still another large disadvantage, viz. in order to obtain red emission the larger part of the broad band emission of this phosphor is situated in the near infrared. The maximum of the emission band is close to 680 nm. This implies that the lumen equivalent of this phosphor is low (25%). For $Y_2O_2S:Eu^{3+}$ with line emission this is 55% [1].

Long ago it was predicted that color television with a satisfying brightness would only be possible with a phosphor which emits in the red by line emission around 610 nm [2]. Now we know that only the Eu^{3+} ion is able to satisfy this requirement. In fact the introduction of Eu^{3+}-activated phosphors in the color-television tube was a breakthrough: not just the red, but the total brightness increased strongly. It was also the introduction of rare-earth phosphors leading to many other improvements (e.g. in luminescent lamps) and the end of the domination of the sulfides.

7.3.2 Phosphors for Black-and-White Television [3]

In a sense this is a historical paragraph. The color preferred for black-and-white television is bluish-white. This can be realized by many combinations of two phosphors as prescribed by the chromaticity diagram. The best is $ZnS:Ag^+$ and (yellow-emitting) $Zn_{0.5}Cd_{0.5}S:Ag^+$ or $Zn_{0.9}Cd_{0.1}S:Cu,Al$. Single-component white phosphors have also been found, but none has found practical application.

7.3.3 Phosphors for Color Television

We will discuss the possible materials for the blue- , the green- , and the red-emitting phosphor in turn. For the blue the phosphor $ZnS:Ag^+$ has been continuously in use. As mentioned above, its radiant efficiency is very high and close to the theoretical limit. In Fig. 7.5 its emission spectrum is given.

The emission of $ZnS:Ag^+$ is of the donor-acceptor pair type (see Sect. 3.3.9). Silver is an acceptor in ZnS. The donor is shallow and can be aluminium or chlorine (on zinc or sulfur sites, respectively). The energy level scheme is given in Fig. 7.6.

For the green the sulphide ZnS : Cu,Cl (or Al) is used. This has also an emission of the donor-acceptor pair type, but the copper acceptor levels are located at higher energy above the valence band than those of silver. This yields for copper an emission band with a maximum at 530 nm. For practical reasons it is profitable to shift the

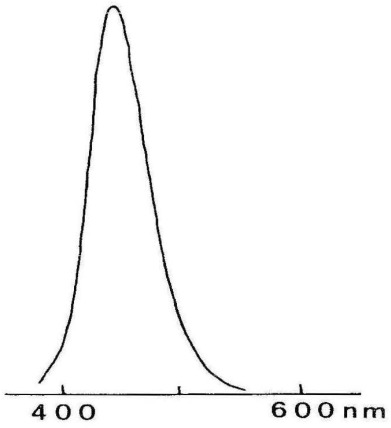

Fig. 7.5. Emission spectrum of the blue-emitting cathode-ray phosphor ZnS : Ag

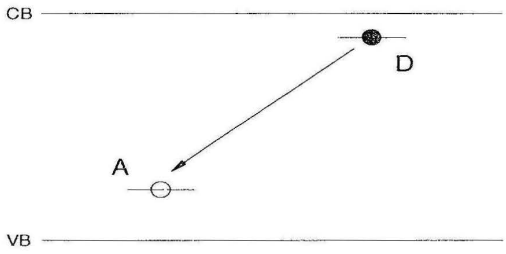

Fig. 7.6. Energy level scheme for the donor-acceptor pair emission of ZnS : Ag. The valence and conduction bands of ZnS are indicated by *VB* and *CB*, respectively. *D* is the shallow donor (aluminium or chlorine), *A* is the acceptor (silver)

emission maximum to a slightly longer wavelength. This can be done by replacing part of the zinc ($\sim$ 7%) by cadmium, or by adding a deeper acceptor such as gold. The emission color depends critically on the defect chemistry of the system [4].

For the red-emitting phosphor originally (Zn,Cd)S : Ag and $Zn_3(PO_4)_2 : Mn^{2+}$ have been used. After the prediction that the red emission should consist of a narrow emission around 610 nm [2], it took another 10 years before Levine and Palilla [5] proposed $YVO_4 : Eu^{3+}$ as the red phosphor for color television tubes. This interesting material has already been discussed before (Sects. 5.3.2 and 6.4.3). A few years later it was replaced by $Y_2O_2S : Eu^{3+}$ which gave increased brightness [6]. This host lattice will reappear in the chapter on X-ray phosphors. Many years later Kano et al. proposed $Y_2(WO_4)_3 : Eu^{3+}$ because of its high lumen equivalent [7].

The great succes of the Eu^{3+} luminescence in this aspect is illustrated in Fig. 7.7. This shows the eye sensitivity curve which drops sharply in the red spectral area, and the emission spectra of a Eu^{3+}-activated phosphor and red-emitting (Zn,Cd)S : Ag. It is clear that the main part of the emission of the sulfide lies outside the eye sensitivity

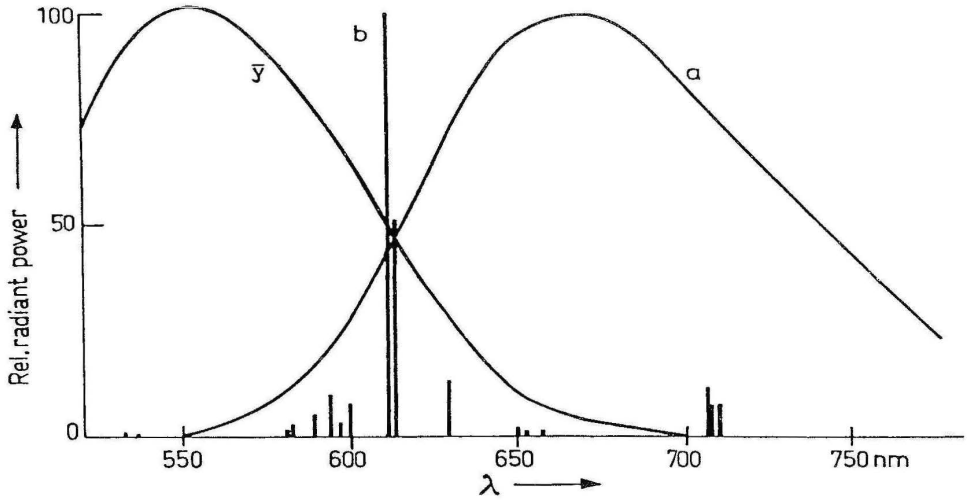

Fig. 7.7. (*a*) Emission spectrum of red-emitting (Zn,Cd)S : Ag. (*b*) emission spectrum of a red-emitting Eu^{3+} phosphor. ($\bar{y}$): eye-sensitivity curve

Table 7.1. Luminescent properties of red-emitting cathode-ray phosphors (after Ref. [1]).

Phosphor	Radiant efficiency (%)	L*	Relative brightness
$Zn_3(PO_4)_2 : Mn^{2+}$	6.7	47	39
(Zn,Cd)S : Ag	16	25	51
$YVO_4 : Eu^{3+}$	7	62	55
$Y_2O_3 : Eu^{3+}$	8.7	70	88
$Y_2O_2S : Eu^{3+}$	13	55	100
$Y_2(WO_4)_3 : Eu^{3+}$	4.3	81	46
611 nm radiation		100	

* Lumen equivalent relative to monochromatic light of 611 nm wavelength.

curve, so that the lumen equivalent is low. Table 7.1 gives a survey of the red-emitting cathode-ray phosphors with their properties.

It is important that the $^5D_0 - ^7F_4$ emission of Eu^{3+} at about 700 nm is as weak as possible, since this will decrease the lumen equivalent. The high value of the lumen equivalents of $Y_2O_3 : Eu^{3+}$ and $Y_2(WO_4)_3 : Eu^{3+}$ are actually due to the low $^5D_0 - ^7F_4$ intensity. Further, the $^5D_1$ emission of Eu^{3+} should be quenched by cross relaxation as in the lamp phosphor (see Sect. 6.4.1.4). This makes a Eu^{3+} concentration of some 3% necessary.

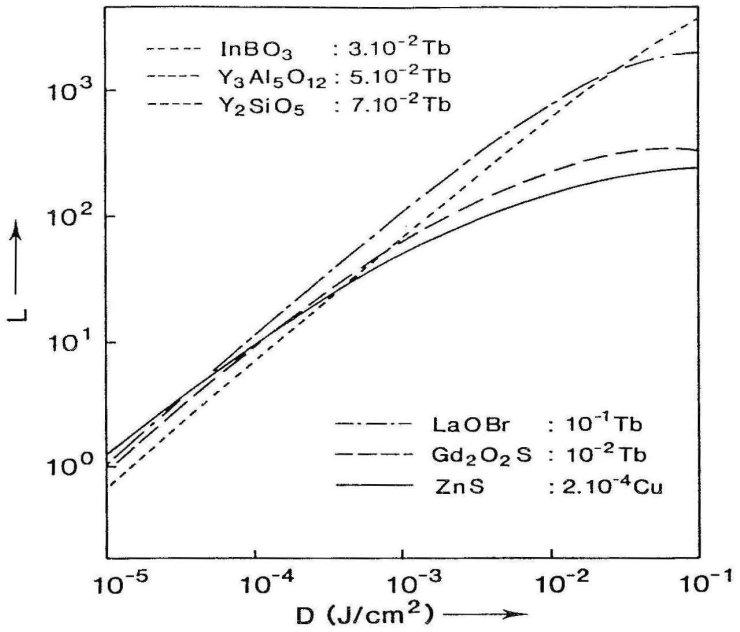

Fig. 7.8. Non-linearity of green PTV phosphors

7.3.4 Phosphors for Projection Television

As argued in Sect. 7.1 one of the problems with cathode-ray phosphors in projection television is the saturation of their light output under high excitation density. Related to this is the temperature increase of the phosphor under these circumstances: the screen temperature can rise to 100°C [8].

The nonlinear behavior of the light output was originally ascribed to ground state depletion of the activator. In sulfides, where the activator concentration is low (~ 0.01%), this is certainly important. Therefore, attention shifted to the oxidic phosphors where the activator concentrations are much higher (~ 1%). However, excited state absorption and Auger processes (Sect. 4.6) will also result in saturation effects. Detailed analysis of interactions between excited activator ions are available [9,10].

In Fig. 7.8 the light output of a number of green-emitting phosphors is plotted versus the density of cathode-ray excitation. In Fig. 7.9 their temperature dependence is given. Although the sulfide has the highest radiant efficiency at low excitation densities, viz. 20%, it shows a pronounced saturation. Note also the drop in light output upon increasing the temperature.

The Tb^{3+}-activated materials perform much better with the exception of $Gd_2O_2S:Tb^{3+}$. The bad performance of the latter seems to be due to its bad temperature dependence.

Serious candidates for application as a green phosphor in PTV tubes are $Y_2SiO_5:Tb^{3+}$, $Y_3Al_5O_{12}:Tb^{3+}$ and $Y_3(Al,Ga)_5O_{12}:Tb^{3+}$. The phosphor $InBO_3:Tb^{3+}$ is excellent from several points of view, but its decay time is very long, viz. 7.5 ms

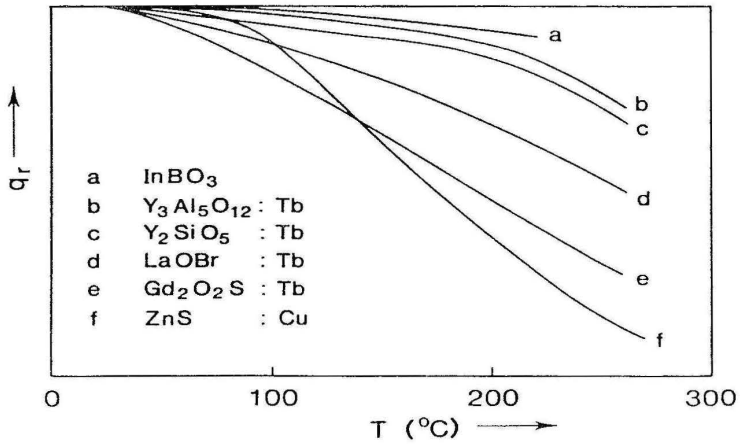

Fig. 7.9. Thermal quenching of the green emission of some cathode-ray phosphors

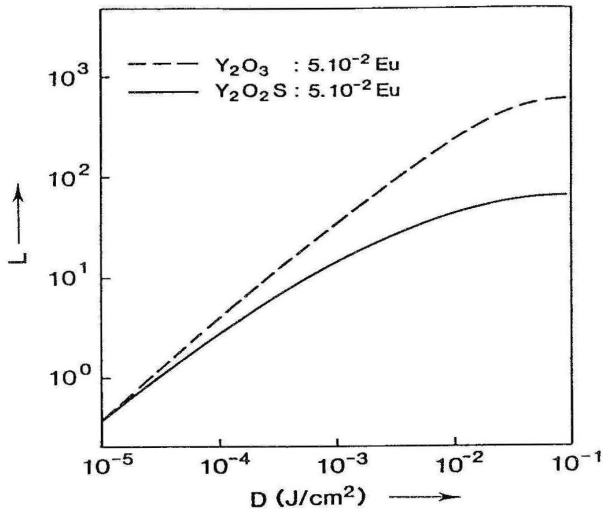

Fig. 7.10. Non-linearity of the red cathode-ray phosphors. Figs. 7.8–7.10 are reproduced with permission from Ref. [14]

[8]. This is due to the calcite structure of $InBO_3$ which places Tb^{3+} on a site with inversion symmetry which forbids the forced electric-dipole transitions (Sect. 2.3.3). An important criterion in the final phosphor selection is their degradation behavior in the tubes under high-density excitation [11].

The red phosphor in PTV tubes is usually $Y_2O_3:Eu^{3+}$, because $Y_2O_2S:Eu^{3+}$ shows saturation (see Fig. 7.10). The properties of $Y_2O_3:Eu^{3+}$ were discussed in Sect. 6.4.1.4.

An ideal blue phosphor for PTV tubes has not yet been found. Materials activated with Eu^{2+} suffer from severe degradation. The Ce^{3+} emission in (La,Y)OBr and (La,Gd)OBr is attractive, but the host lattice is unfavorable for screen making

[12]. The Tm^{3+} ion can give blue emission, but cross-relaxation limits the activator concentration, so that saturation occurs. In spite of its saturation at high excitation densities, the old $ZnS:Ag^{+}$ has not yet been surpassed under these conditions. As a consequence the screen brightness is limited by the blue-emitting phosphor. Extensive research by many laboratories has not changed this situation.

7.3.5 Other Cathode-Ray Phosphors

In the literature many other cathode-ray phosphors are known for several purposes. Two of these we will mention here, partly because they are generally known as luminescent materials, partly because their properties are also interesting from a fundamental point of view. They are $Zn_2SiO_4:Mn^{2+}$, also known by the mineral name willemite, and the family of Ce^{3+}-activated phosphors. Still more cathode-ray phosphors can be found in Ref. [1].

The green-emitting phosphor $Zn_2SiO_4:Mn^{2+}$ was also mentioned in the chapter on lamp phosphors. This might suggest that an efficient phosphor can find application everywhere. However, this is by no means true. The halophosphates, for example, are highly efficient under ultraviolet excitation (Chapter 6), but not under cathode rays. The reason for this is that efficient excitation of the activator itself is no guarantee for efficient excitation via the host lattice. However, if an activator can be efficiently excited via the host lattice, it can also be efficiently excited directly. In addition, when ultraviolet irradiation excites the host lattice, the efficiency of this excitation and cathode-ray excitation will run parallel. An illustration of the latter is formed by the sulfides and $YVO_4:Eu^{3+}$; an illustration of the former is $Y_2O_3:Eu^{3+}$ (compare the discussion in Sect. 2.1).

Willemite is used as a cathode-ray phosphor in terminal displays and oscilloscope tubes. The decay time is very long, viz. 25 ms [1]. This is mainly due to the spin- and parity- forbidden nature of the $^4T_1 \rightarrow {}^6A_1$ emission transition in the $3d^5$ configuration of the Mn^{2+} ion (Sect. 3.3.4.c), but there is also a contribution of afterglow. An even longer persistance is observed for samples to which As has been added. As a result of the As addition, electron traps are formed which trap the electrons for a certain time, so that the emission is delayed (Sect. 3.4).

Cathode-ray phosphors with such a long persistence are suitable to avoid or minimize flicker in the display. This is especially of importance when high-definition figures need to be displayed. For application in television tubes (moving pictures) or high-frequency oscilloscopes, such a long persistence is of course fatal.

The Ce^{3+}-activated cathode-ray phosphors are used in applications where a very short decay time is a requirement [13]. Since the emission is a completely allowed transition ($5d \rightarrow 4f$, Sect. 3.3.3.a), the decay time of Ce^{3+} varies between about 15 and 70 ns, depending on the emission wavelength. One application is in the beam-index tubes which generate color images by means of one electron gun [1,13]. This system could, however, never compete with the above-mentioned shadow-mask tube. The beam-index phosphor indicates the location of the electron beam. Therefore, the emission should have a very short decay time and, in order not to disturbe the image, should be situated in the ultraviolet. A good choice is $Y_2Si_2O_7:Ce^{3+}$ with a radiant

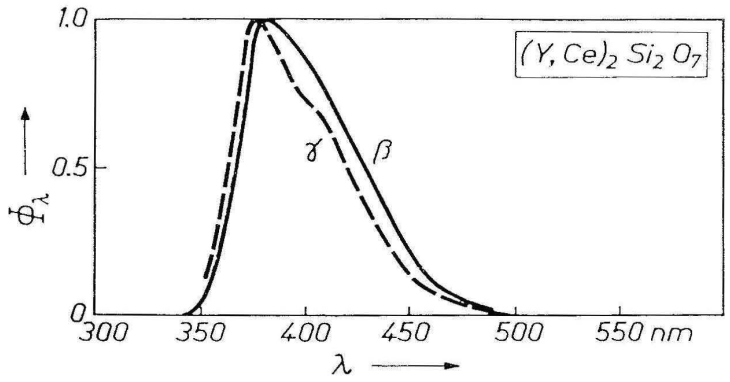

Fig. 7.11. Emission spectra of β- and γ-$Y_2Si_2O_7 : Ce^{3+}$ under cathode-ray excitation (after Ref. [13])

efficiency of some 7% and a decay time of 40 ns. The maximum emission wavelength is 375 nm. Figure 7.11 shows the emission spectra of the β and the γ modifications. Especially the γ modification shows clearly the double emission band character which is due to the splitting of the $4f^1$ ground configuration into the $^2F_{5/2}$ and $^2F_{7/2}$ levels (Sect. 3.3.3.a).

The other application is the flying-spot scanner. In this set up the information of slides or film can be transformed into electric signals. The electron beam excites a phosphor with short decay time. The luminescence signal scans the object point by point and the transmitted radiation is detected with a photomultiplyer. To reduce blurring of the signal, the decay time of the phosphor should be of the order of magnitude of the time the electron beam scans a picture element ($\sim$ 50 ns).

In order to transmit pictures in color, the emission of the phosphor should cover the whole visible area. For this purpose a mixture of $Y_2SiO_5 : Ce^{3+}$ and $Y_3Al_5O_{12} : Ce^{3+}$ has been used. The former emits in the blue, the latter in the green and red [13]. The reason that Ce^{3+} in $Y_3Al_5O_{12}$ emits at such long wavelengths is due to the extended crystal-field splitting of the excited Ce^{3+} ion (i.e. $5d^1$ configuration). This was considered in Sect. 3.3.3.a.

It is interesting to note that $Y_3Al_5O_{12} : Ce^{3+}$ was originally developped for the flying-spot scanner tube [13]. However, today its application lies in the special de luxe lamps as discussed in Sect. 6.4.1.7. For the former application its long wavelength emission with short decay time is essential, for the latter its long wavelength absorption and emission. In both cases the low energy position of the lowest crystal-field component is essential.

7.4 Outlook

The field of cathode-ray phosphors is relatively old and has reached a high level of maturity. The quality of todays color television is a token of the success of these materials. For direct-view television there is not much more to desire as far as the luminescent materials are concerned. The combination $ZnS:Ag^{+}$, $ZnS:Cu^{+},Al^{3+}$, and $Y_2O_2S:Eu^{3+}$ is worldwide considered to be the most suitable combination.

In the fields of projection television phosphors the situation is less satisfactory. It is clear that luminescent materials have difficulties in meeting the high requirements. At the moment the largest need is for a blue-emitting phosphor with an acceptable saturation. The bad situation is well illustrated by the blue phosphor used, viz. $ZnS:Ag^{+}$. Its high radiant efficiency in direct-view television tubes ($\sim$ 20%) decreases to less than 5% under the conditions of the projection-television tube. Nevertheless it has not been possible, up till now, to find an acceptable alternative.

References

1. Hase T, Kano T, Nakazawa E, Yamamoto H (1990) In: Hawkes PW (ed) Advances in electronics and electron physics, vol. 79. Academic, New York, p 271
2. Bril A, Klasens HA (1955) Philips Res. Repts 10:305; Klasens HA, Bril A (1957) Acta Electronica 2:143
3. Ouweltjes JL (1965) Modern materials, vol. 5, Academic, New York, p 161
4. Bredol M, Merikhi J, Ronda C (1992) Ber. Bunsenges. Phys. Chem. 96:1770
5. Levine AK, Palilla FC (1964) Appl. Phys. Letters 5:118
6. Royce MR, Smith AL (1968) Ext. Abstr. Electrochem. Soc. Spring Meeting 34:94; Royce MR (1968) US patent 3.418.246
7. Kano T, Kinameri K, Seki S (1982) J. Electrochem. Soc. 129:2296
8. Welker T (1991) J. Luminescence 48, 49:49
9. de Leeuw DM, 't Hooft GW (1983) J. Luminescence 28:275
10. Klaassen DBM, van Rijn TGM, Vink AT (1989) J. Electrochem. Soc. 136:2732
11. Yamamoto H, Matsukiyo H (1991) J. Luminescence 48,49:43
12. Raue R, Vink AT, Welker T (1989) Philips Techn. Rev. 44:335
13. Bril A, Blasse G, Gomes de Mesquita AH, de Poorter JA (1971) Philips Techn. Rev. 32:125
14. Smets B (1991) In: DiBartolo B (ed) Advances in nonradiative processes in solids, Plenum, New York, p 353

CHAPTER 8

X-Ray Phosphors and Scintillators (Integrating Techniques)

8.1 Introduction

The terms X-ray phosphors and scintillators are often used in an interchangeable way. Some authors use the term X-ray phosphors when the application requires a powder screen, and the term scintillator when a single crystal is required. The physical processes in the luminescence of these two types of materials is, however, in principle the same and comparable to that in cathode ray phosphors (Chapter 7).

Therefore another subdivision of the broad field of X-ray phosphors and scintillators is used here, viz. materials used in applications where integrating techniques are used (Chapter 8), and materials used in applications where counting techniques are used (Chapter 9). The integrating technique measures the light intensity under continuous excitation; it is position sensitive and yields an image; a well-known example is the case of X-ray imaging in medical diagnostics. The counting technique digests the radiation excited by a single pulse; it yields the number of exciting events; a well-known example is the use of scintillators in electromagnetic calorimeters in order to count photons, electrons or other particles.

X-ray phosphors can be defined as materials which absorb X rays and convert the absorbed energy efficiently into luminescence, in practice often ultraviolet or visible emission. In this paragraph we consider the phenomenon of X-ray absorption, and the principles of some important ways of X-ray imaging and the requirements which X-ray phosphors have to satisfy in order to be promising for potential application.

In the next paragraph several aspects of materials preparation are discussed. A complicating factor is formed by the fact that such materials are applied as powders, ceramics or single crystals, depending on the application. In Sect. 8.3, the possible materials are considered following the several applications. The final paragraph presents an outlook into the future of this complicated field of materials research.

8.1.1 X-Ray Absorption

Figure 8.1. shows a schematic picture of the X-ray absorption coefficient a vs the energy E of the X rays. When X rays interact with an atom or ion, they may remove an electron from the K shell if the energy of the X-ray quantum is equal to or larger

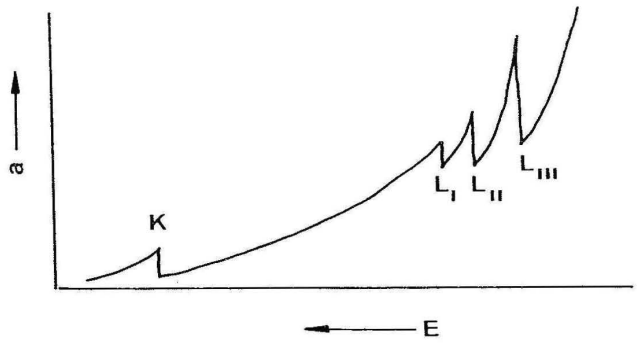

Fig. 8.1. The X-ray absorption coefficient a as a function of the energy E of the X-rays (schematic). The K and L X-ray absorption edges are indicated

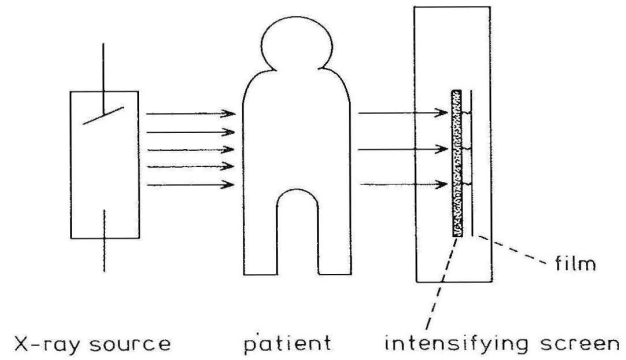

Fig. 8.2. Schematic representation of a medical radiography system based on the use of an intensifying screen

than the binding energy E_K of the K electron. This absorption yields a continuous absorption spectrum starting at E_K and extending to higher energy. This corresponds to the left-hand part of the spectrum in Fig. 8.1.

In a similar way, the weaker-bounded L electrons yield three continuous absorption spectra which start at the energies L_I, L_{II} and L_{III} (Fig. 8.2., right-hand side). Even weaker-bounded electrons (M shell, and so on) yield absorption edges at still lower energy, depending on the atomic number.

The absorption coefficient increases strongly with the atomic number. As a consequence X-ray phosphors will necessarily contain heavy elements; another way to formulate this requirement is that X-ray phosphors must be high-density materials.

8.1.2 The Conventional Intensifying Screen

After the discovery of X rays in 1895, Röntgen realized immediately that X rays are not efficiently detected by photographic film. The reason for this is the weak

absorption of X rays by such a film. In this way long irradiation times would be required which results in vague pictures when the object moves (like the human body generally does). In addition the negative influence of X-ray irradiation on the human body is nowadays sufficiently known. Immediately after Röntgen's invention a search for phosphors which were able to absorb X rays and to convert the absorbed energy efficiently into light was started [1]. As early as one year later, in 1896, Pupin proposed $CaWO_4$ for this purpose This material served for some 75 years in the so-called X-ray intensifying screens, an absolute record for a luminescent material. In this way the irradiation time was reduced by about three orders of magnitude! The luminescence properties of $CaWO_4$ have already been discussed (see Chapter 1, and Sects 3.3.5 and 5.3.2).

A medical radiography system based on the use of an intensifying screen is represented in Fig. 8.2. The X-ray radiation transmitted by the patient is detected by the X-ray phosphor which is applied as a screen. The emitted luminescence is detected by photographic film. The spectral film sensitivity should coincide optimally with the spectral energy distribution of the emitted luminescence. Although the medical application of this principle is best known, other applications are also in use. An example is nondestructive materials control.

A more realistic picture of the X-ray cassette is given in Fig. 8.3. It is seen that the film is surrounded on both sides by an intensifying screen for optimal sensitivity. This figure also shows the disadvantage of the intensifying screen, viz. it causes a certain blur which impairs the definition of the image. This is due to the fact that the direction of the light emission is independent of the angle of incidence of the X-ray photon, so that the emission diverges in all directions. This is worse, since the

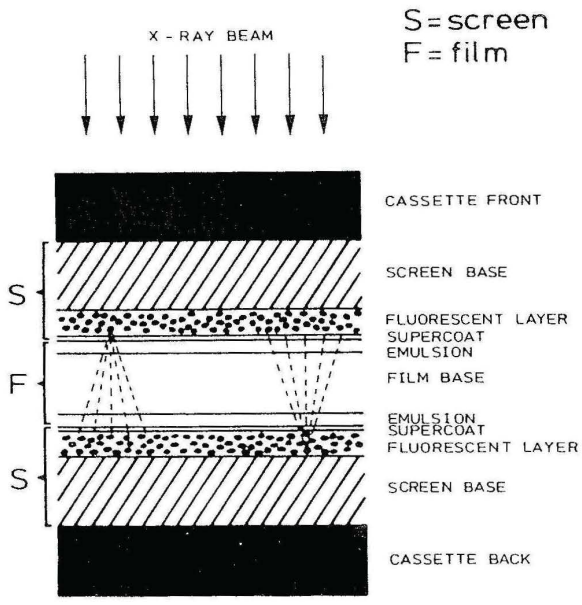

Fig. 8.3. Section through an X-ray cassette containing a double-coated film (*F*) and a pair of intensifying screens (*S*)

diffusing emission light reaches not only the film side adjacent to the emitting screen, but also that remote from the screen (see Fig. 8.3). This is known as the cross-over effect. Occasionally radiologists prefer, therefore, to make X-ray images without an intensifying screen. This is sometimes possible, for example, for an image of the hand which is a non-moving object.

Of course the packing and the size of the crystallites in the screen and the thickness of the screen are another source of unsharpness in the image. It is obvious that the smaller the crystal size, the closer the packing, and the thinner the screen layer is, the better the sharpness will be.

From this discussion it will be clear that the requirements for X-ray phosphors to be used in intensifying screens are the following: high X-ray absorption and high density, a high conversion efficiency for X-ray to light conversion, an emission spectrum which covers the film sensitivity (in practice blue or green), stability, and an acceptable cost price. The factors determining a high conversion efficiency were discussed in Sect. 4.4. Although $CaWO_4$ has been used for a long time, it did not satisfy these requirements, as we will see below. It has been replaced by rare-earth doped materials.

8.1.3 The Photostimulable Storage Phosphor Screen

About ten years ago the Japanese Fuji corporation introduced a new technique for X-ray imaging [2]. This technique is based on the use of a photostimulable storage phosphor screen. The operation of a storage phosphor is depicted schematically in Fig. 8.4. Upon irradiation electrons are promoted from the valence band to the conduction band. In a storage phosphor a number of the created free charge carriers are trapped in electron traps and hole traps. The traps are localized energy states in the bandgap due to impurities or lattice defects. If the trap depth ΔE is large compared to kT, the probability for thermal escape from the trap will be negligibly small and a metastable situation is created.

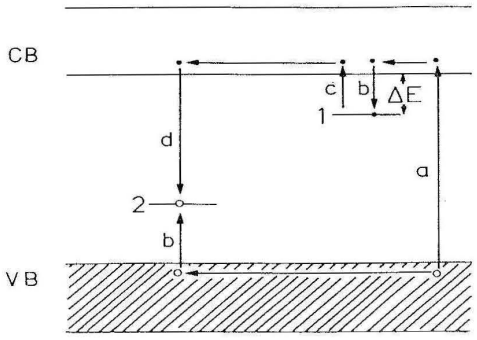

Fig. 8.4. Energy band model showing the electronic transitions in a storage phosphor: (*a*) generation of electrons and holes; (*b*) electron and hole trapping; (*c*) electron release due to stimulation; (*d*) recombination. Solid circles are electrons, open circles are holes. Center 1 presents an electron trap, center 2 a hole trap

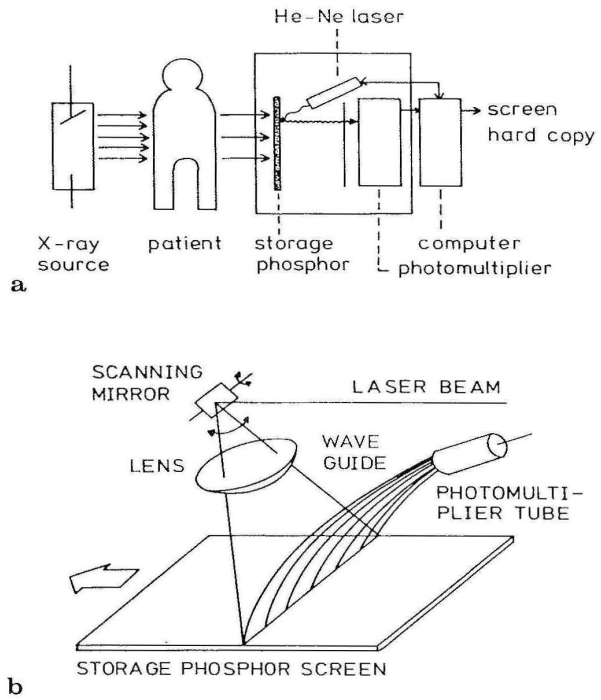

Fig. 8.5. (*a*) Schematic representation of a medical radiography system based on the use of a photostimulable storage phosphor. (*b*) The image reader in greater detail. Figures 8.2, 8.4 and 8.5 are from A. Meijerink, thesis, University Utrecht, 1990

The stored energy can be released by thermal or optical stimulation. In the case of thermal stimulation the irradiated phosphor is heated to a temperature at which the energy barrier ΔE can be overcome thermally. The trapped electron (or hole) can escape from the trap and recombine with the trapped hole (or electron). In the case of radiative recombination, luminescence is observed which is called thermally stimulated luminescence (TSL) (compare Sect. 3.5). Under optical stimulation the energy of an incident photon is used to overcome ΔE. The luminescence due to optical stimulation is called photostimulated luminescence (PSL). The phenomenon of stimulated luminescence from storage phosphors has been known since 1663 (Boyle)[2]. Storage phosphors have found a wide range of applications, e.g. as infrared detectors and in the field of dosimetry [3].

The X-ray imaging system based on a photostimulable storage phosphor is depicted in Fig. 8.5. The X-ray film is replaced by a storage phosphor screen as a primary image receptor. The transmitted X-ray photons are absorbed by the storage phosphor in the screen, where a dose-proportional amount of energy is stored. The latent image in the screen is read out by scanning the phosphor screen with a focussed

2 Boyle reported in the Register of the Royal Society (1663) 213 "a glimmering light from diamond by taking it to bed with me and holding it a good while upon a warm part of my naked body".

He–Ne laser. The red laser light ($\lambda = 633$ nm) stimulates recombination, resulting in photostimulated luminescence. The intensity of the photostimulated luminescence is proportional to the X-ray dose. For each spot of the laser beam on the screen the intensity of the photostimulated luminescence is measured by a photomultiplier tube and stored in a computer. The X-ray photograph in the computer can be visualized on a monitor or by making a hard copy.

This new technique for X-ray imaging offers several important advantages over conventional screen-film radiography. The response of the system is linear over at least four decades of the X-ray dose ($10^{-2} - 10^{2}$ mR). This wide dynamic range prevents overexposure and underexposure. The sensitivity of the system is higher due to a higher sensitivity of the photomultiplier tube to light compared to film. The higher sensitivity enables a reduction of the exposure time. Finally, the digitized images obtained with this system can be processed by a computer which offers the possibility of digital manipulation and facilitates archiving.

Apart from the high price, the main disadvantage of the digital X-ray imaging system is the lower resolution. Due to scattering of the laser beam the performance of the system is worse than the performance of the conventional screen-film system. This prohibits application in areas where a high resolution is required. The development of a translucent storage phosphor screen with minimal scattering could solve this problem.

A good storage phosphor has to meet a number of requirements:

a. The absorption coefficient for X-rays must be high. This can be achieved by using materials with a high density.
b. The amount of energy stored in the phosphor per unit X-ray dose has to be large in order to obtain high sensitivity.
c. A short decay time (< 10 μs) of the photostimulated emission is required for a fast readout.
d. The fading of the information stored in the phosphor has to be slow (preferably the information must still be present several hours after exposure).
e. Stimulation has to be possible in the red or near infrared. The stimulated emission has to be located between 300 and 500 nm where the photomultiplier tube has its highest sensitivity.

The photostimulable phosphor used at present in nearly all commercial digital X-ray imaging systems is $BaFBr:Eu^{2+}$. A physical mechanism for the PSL in Eu^{2+}-activated barium fluorohalides has been proposed by Takahashi et al. [4]. Optical, EPR and photoconductivity studies indicate that upon X-ray irradiation some of the holes are trapped by Eu^{2+} ions, giving Eu^{3+}, and some of the electrons in halide vacancies, giving F centers. Illumination in the F-center absorption band stimulates recombination of the trapped electron with the hole trapped on Eu^{2+}, resulting in Eu^{2+} in the excited $4f^{6}5d$ state. The Eu^{2+} ion returns to the ground state radiatively and the characteristic Eu^{2+} emission around 390 nm is observed.

It was soon realised that the simple scheme of Fig. 8.4 is a simplification. Studies on the recombination mechanism suggest that electron-hole recombination in $BaFBr:Eu^{2+}$ does not take place via an electron entering the conduction band, but via tunnelling. The evidence for this originates from different sources [5]:

a. the decay of the photostimulated luminescence under continuous stimulation in the temperature region 100–300 K is found to be temperature independent
b. the increase of the photostimulated luminescence intensity with increasing X-ray dose appears to be linear which points to a tunnelling process
c. analysis of the thermally stimulated luminescence points also to tunnelling.

An important contribution to the theoretical model formation originates from the use of vacuum-ultraviolet radiation from a synchrotron source [6]. It was shown that photostimulable centers in BaFBr : Eu^{2+} can be created by irradiation into the vacuum-ultraviolet region (> 6.7 eV), i.e. in the excitonic and interband region of the host lattice.

The model originating from this work invokes, as a first step, the relaxation of a free exciton in the neighbourhood of a lattice distortion induced by Eu^{2+}. This leads to an $e+V_K$ centre (where e stands for electron, and V_K for the V_K hole center consisting of a Br_2^- molecule on two Br^- sites). Subsequently an off-center self-trapped exciton is formed, viz. a nearest-neighbor F–H pair (where F is the well-known F center, in which an electron is trapped at an anion vacancy, and H is the H center, which can be regarded as an X_2^- molecule occupying an X^- anion site; the anion concerned here is Br^-; see also Sect. 3.3.1). This pair is assumed to be stabilized by the presence of a substitutional Eu^{2+} ion which is much smaller than Ba^{2+}. The photostimulable center is then a Eu^{2+}–F–H complex.

Photostimulation is thought to occur as follows: upon excitation, the F center induces a certain relaxation which destabilizes the H center and an excited $e + V_K$ center is formed. The excitation energy is transferred to the nearby Eu^{2+} ion and emission follows. This model also accounts for the fact that practically no Eu^{3+} has been observed after X-ray irradiation of BaFBr : Eu^{2+}. Note that the simple model of Fig. 8.4 requires the presence of Eu^{3+} after irradiation.

Interestingly enough, Koschnick et al. [7] have presented convincing experimental evidence from cross-relaxation spectroscopy which shows that the PSL center in BaFBr : Eu^{2+} consists of a spatially correlated but undistorted F center, an O_F^x center and a Eu_{Ba}^x center. Since x indicates neutral relative to the lattice, O_F^x indicates a hole trapped on oxygen, and Eu_{Ba}^x a Eu^{2+} ion on a barium site. The oxygen is present as an impurity in the lattice. These results illustrate how difficult it is to unravel the storage mechanism in a simple compound like BaFBr. Since the latter studies were performed on crystals with low Eu concentrations, it cannot be excluded that in the powder particles in a screen the mechanism is different. In the other proposed storage phosphors the mechanism may again be different. Therefore we conclude that many details of the storage mechanism in X-ray phosphors are still unknown.

Apart from the application of X-ray storage phosphors in medical diagnostics, there are other applications foreseen [8]. Among these are the use of storage phosphors in (protein) crystallography and in the field of data storage.

8.1.4 Computed Tomography

By means of X-ray computed tomography (CT) it is possible to construct excellent cross-sectional images of the human body and head. Figure 8.6 gives some impressive examples. The prototype was introduced by Houndsfield in 1972 [9]. In such a system the X-ray tube and the detector are rigidly coupled and rotate around the patient (rotation-rotation principle) during the scan. During this rotation, a planar, fan-shaped beam of X-rays passes through a cross-sectional slice of the patients body and strikes the detector system. The principle is shown in Fig. 8.7. During the scan the tube-detector-system characteristically executes a 360° rotation within 1 to 2 seconds. This fan beam consists of as many individual beams as there are detector elements, nowadays normally 768 single detectors [10].

In order to be able to construct CT images, attenuation profiles of that part of the object located in the measurement field are scanned from several different viewing directions. The scanned object is continuously irradiated during the measurement. The 768 detector channels generate electrical signals corresponding to the actual beam attenuation, which are queried in rapid sequences by the detector electronics, and digitized and transmitted to the image processor.

The width of the detector elements, and the geometric arrangement of the X-ray source, the collimation and the detector determine together the spatial resolution of the system, which is at present 0.4 mm. Computed tomography detectors are operating in current mode due to a dose flux in the range of 1 R/s, which yields quanta rates up to 10^{10} s^{-1}.

The quantitative determination of X-ray intensities with a photon energy up to 150 keV can be realized by three types of detectors: semiconductor-based detectors which call for efficient cooling, ionization chambers which have a low quantum detection efficiency ($< 50\%$), and detectors based on luminescent materials. The latter type of detector is of interest here, because it is realized by the combination of a luminescent material with a photodiode.

In the array of 768 individual detectors, each element is about one millimeter wide. The spacing between the elements is rather small, but is present to suppress cross talk by interstitials. Such a detector is shown in principle in Fig. 8.8. The X rays absorbed by the phosphor material are converted into visible light, which is detected by the coupled photodiode. The electrical signal is generated by photoelectric conversion.

The key feature of CT is not the spatial resolution but the contrast resolution, which should have an accuracy of a few parts per thousand. Very small differences in X-ray attenuation which are in general a few percent for soft tissue parts have to be detected precisely, while simultaneously CT must be able to detect the highest attenuation in the case of bone material. With modern CT installations, a few parts per thousand are recognized within a high dynamic range of up to 10^6. Therefore, the properties of a suitable CT phosphor have to satisfy the following requirements [11]:

a) The absorption coefficient should be high. This can be realized by looking for compounds which contain elements of a high atomic number, usually > 50, and a high density, > 4 g cm^{-3}.

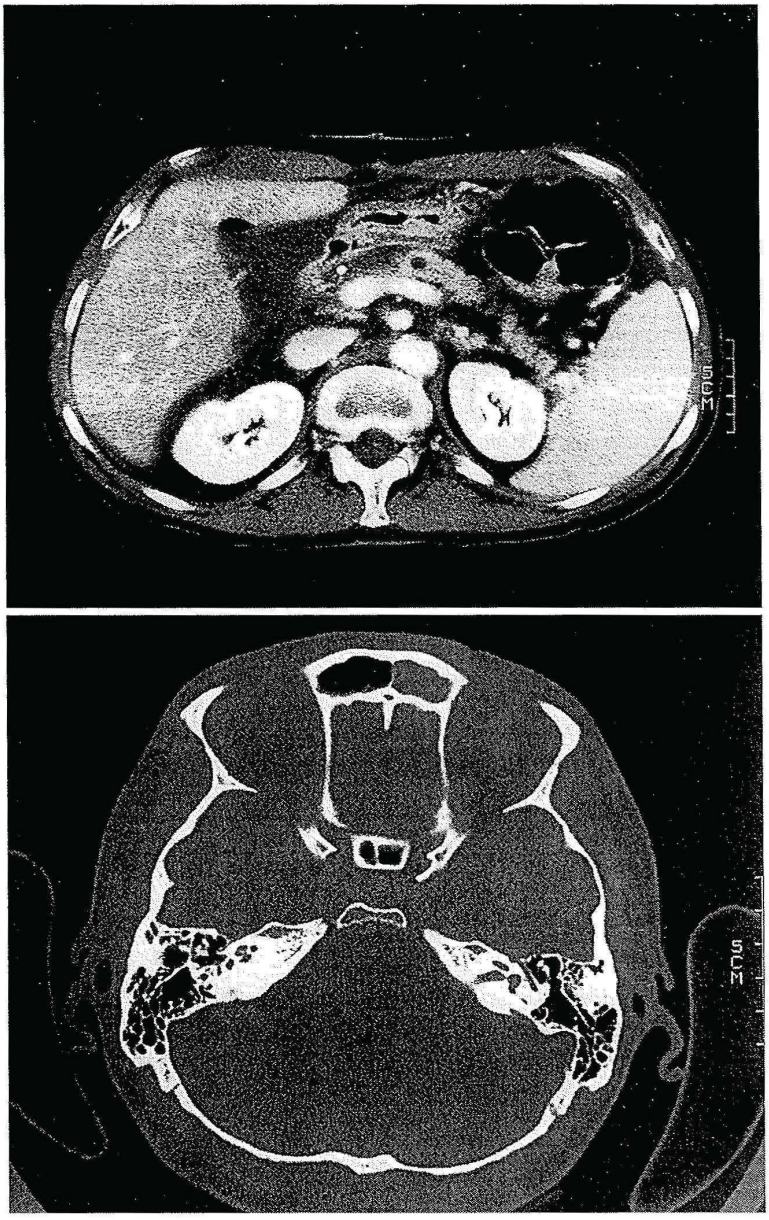

Fig. 8.6. Computed tomography images of the abdomen (top) and of the head (base of the skull) (bottom)

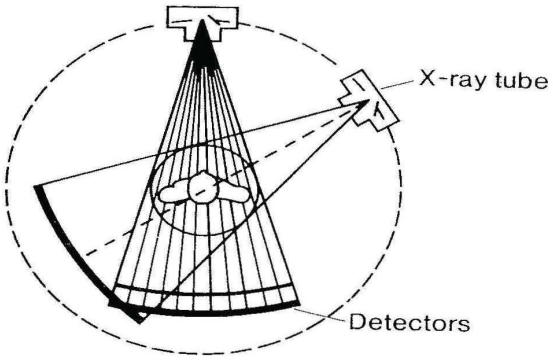

Fig. 8.7. Scanning system of X-ray CT with fan-beam design and rotation principle

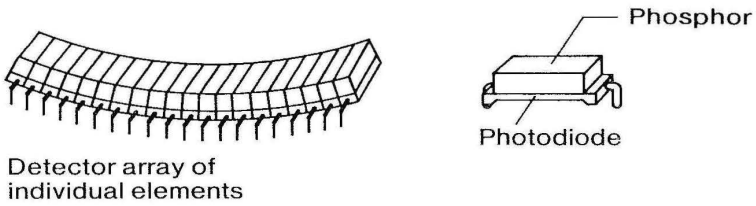

Fig. 8.8. Solid state detector scanner for CT

b) The light output should be high as a result of a high X-ray conversion efficiency and of the interior optical quality. Because the luminescent material is coupled to a Si photodiode, the emission wavelength should be close to the maximum of the sensitivity of the diode in order to ensure high signal conversion.
c) The termination of the emission after X-ray excitation should be fast, i.e. the decay time of the luminescent center has to be short, normally less than 100 microseconds.
d) The afterglow level (Sect. 3.4) should be low. If the afterglow intensities exceed specific limitations, image degeneration occurs due to memory effects. Such limitations are given by the scanning duration of the CT imaging, and should be smaller than 0.01% after 3 milliseconds.
e) Radiation damage effects should be negligibly small. The primary effect of the radiation damage is degradation in transparency rather than in luminescence.
f) Last but not least the suitable phosphor has to satisfy a number of technical requirements, concerning for example, toxicity, chemical stability, reproducibility and machining possibilities.

8.2 Preparation of X-Ray Phosphors

8.2.1 Powder Screens

Much of what has been said before about the preparation of lamp phosphors (Sect. 6.3) and cathode-ray phosphors (Sect. 7.2), is also true for X-ray phosphors from which screens are produced. Brixner [1] has described several preparation procedures. Here we give some examples.

$CaWO_4$ can be readily made via the reaction $Na_2WO_4 + CaCl_2 \rightarrow CaWO_4 + 2NaCl$. The sodium chloride formed acts as a flux to produce nice polyhedral particles of about 0.2–0.3 m^2/g surface area and an average particle size of 5–10 μ. A picture was given before (Fig. 1.7). This is a desirable particle size range, since smaller particles will lose emission intensity via internal scattering and larger particles begin to cause difficulty in making smooth thin screens. The morphology of the phosphor particles is of extreme importance. Ideally, one would like to have nearly spherical, polyhedral particles with some distribution in size. This guarantees optimal packing.

$BaFCl : Eu^{2+}$ is made from BaF_2 and $BaCl_2$ with a europium dopant via solid state reaction. Because of the layered crystal structure (see Fig. 8.9), the morphology of BaFCl crystals is plate-like and very anisotropic. Such plates pack poorly in a screen and there is a tendency for light piping towards the sides of the plates. Spray drying significantly improves the morphology. A similar problem occurs with LaOBr with the same crystal structure.

The oxysulfides Ln_2O_2S (Ln = lanthanide) (see also Sect. 7.3) are also used as X-ray phosphors. The phosphor crystallizes in nearly perfect polyhedra. Figure 8.10 gives an example for $Gd_2O_2S : Tb^{3+}$.

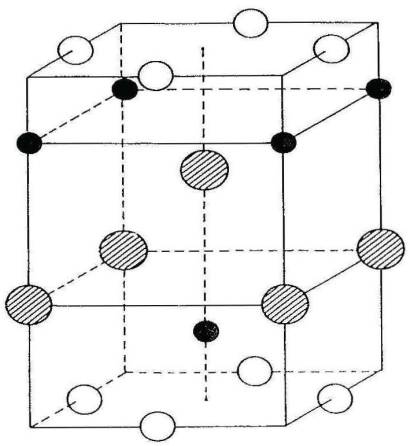

Fig. 8.9. The crystal structure of BaFCl and BaFBr. Black ions are Ba^{2+}, open ions are F^-, and hatched ions are $Cl^-(Br^-)$

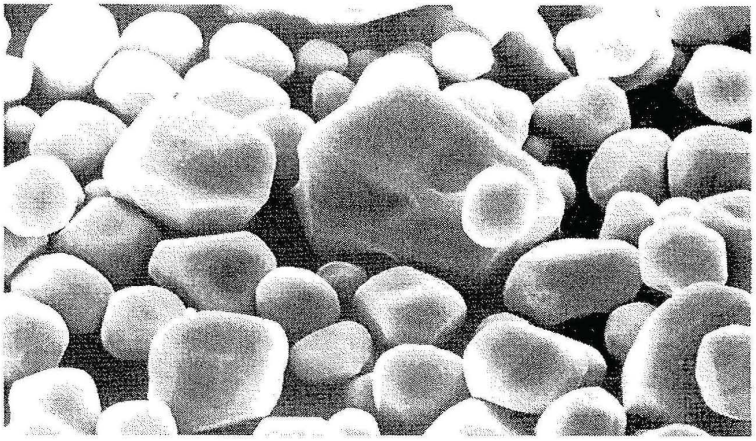

Fig. 8.10. SEM picture of the X-ray phosphor $Gd_2O_2S:Tb^{3+}$ (2500x)

8.2.2 Ceramic Plates

Within the last few years a new class of scintillators based on ceramic materials has been developed. Such ceramic scintillators are polycrystalline, inorganic, nonmetallic solids. These ceramic plates seem to be very promising for computed tomography.

The preparational route for these luminescent ceramics follows the known ceramic technologies [12,13]. They are generated by thermally induced diffusion densification of powder aggregates below their melting temperature, which is referred to as sintering. As a consequence of this preparational route the properties of such ceramic scintillators are not only determined by the host lattice and the dopants (like the luminescent activator), but additionally by the processing technique.

In contrast to conventional phosphor powders, ceramic powder synthesis aims at the generation of powders with highly sinteractive surfaces with particle sizes down to the submicron range and specific surface areas of up to 50 m^2/g. In addition, homogeneous doping on a molecular scale is of substantial importance.

For powder synthesis a large variety of methods is available, for example mixed-oxide solution precipitation or emulsion precipitation. Figure 8.11 shows as an example a $(Y,Gd)_2O_3$ powder prepared by three different precipitation techniques. The powders obtained are different in particle morphology as well as in particle size. Powders prepared by the citrate and the oxalate precipitation techniques are strongly agglomerated [14]. From powders derived in this way, compacts are formed. These powder compacts demonstrate total luminescent properties, but have still low light output due to the high porosity of about 50 vol.%.

This porosity can be reduced by a sintering process at elevated temperature. To achieve complete densification, specific sintering techniques such as vacuum sintering, hot pressing or isostatic gas pressure sintering are necessary. Figure 8.12 gives an example of a dense ceramic specimen with a homogeneous structure [15].

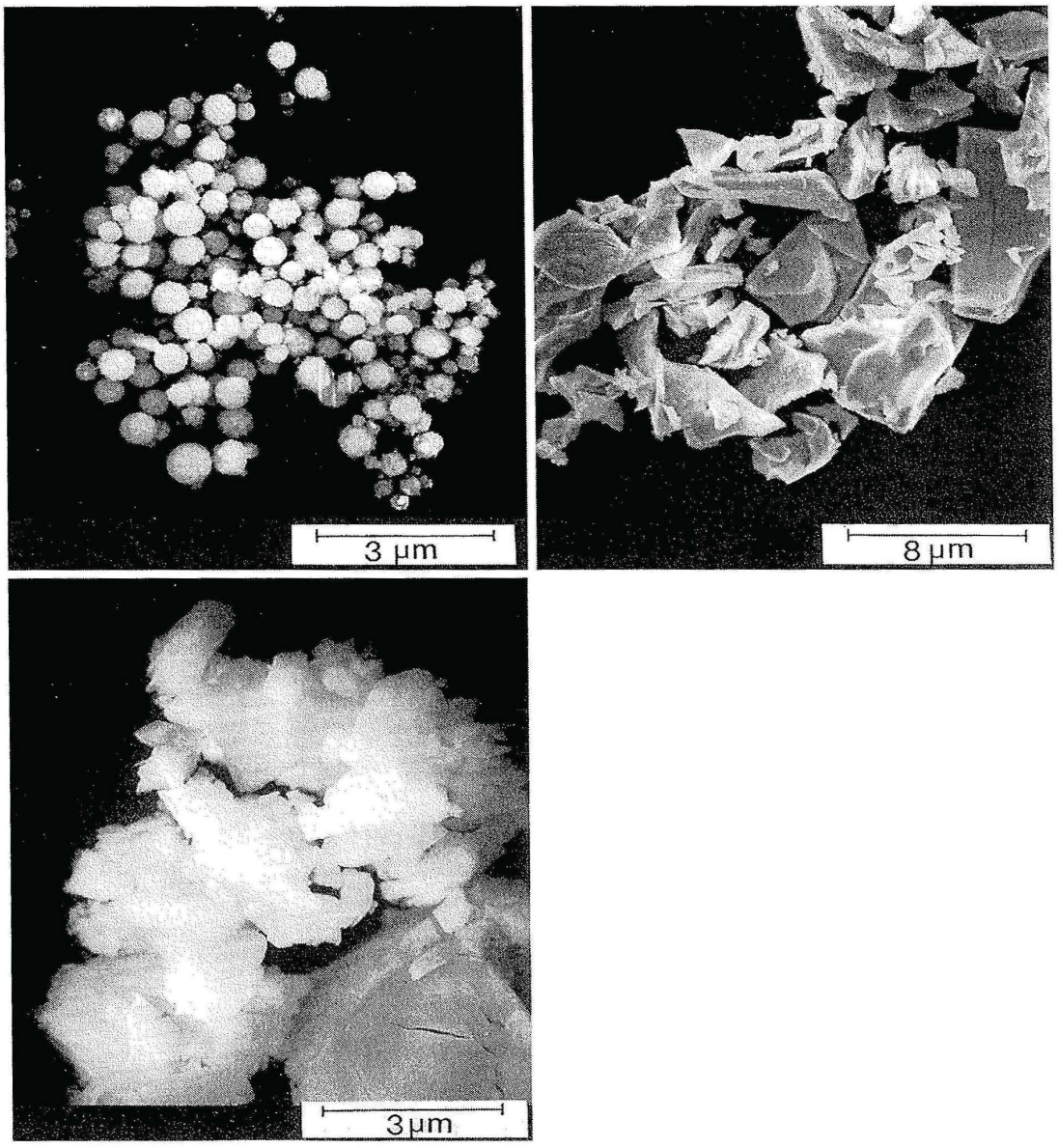

Fig. 8.11. Micrograph of $(Y,Gd)_2O_3$ powders prepared by emulsion precipitation, citrate precipitation and oxalate precipitation (from left to right and bottom).

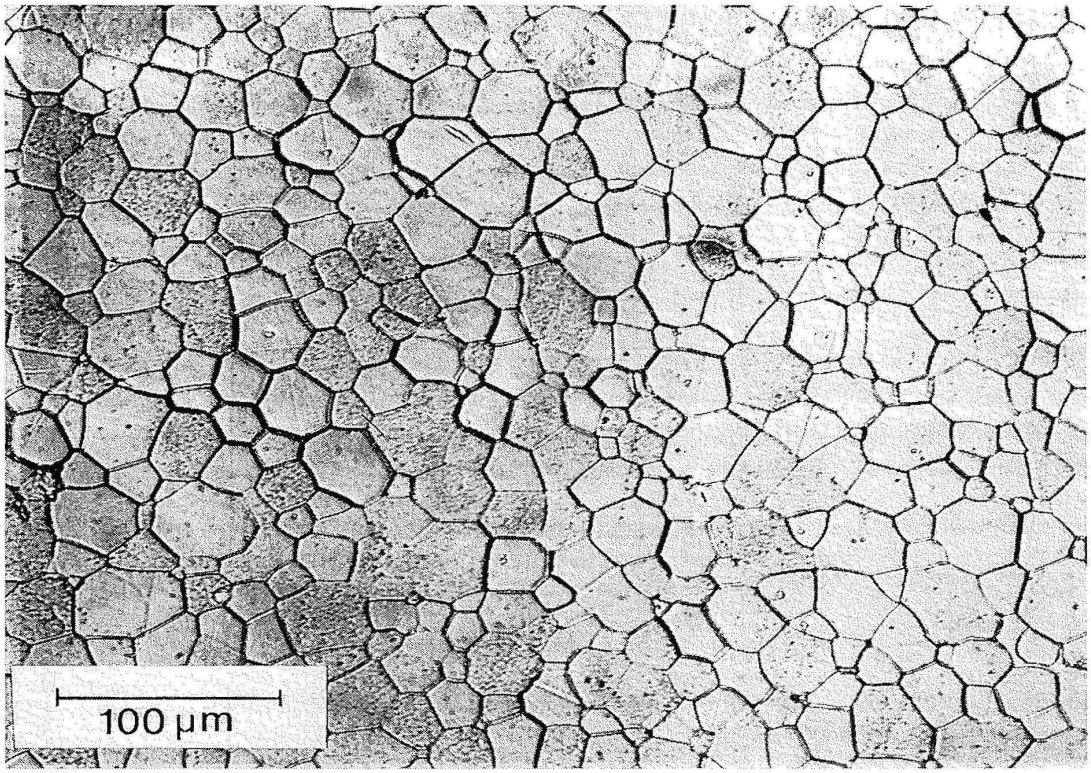

Fig. 8.12. Microstructure of a $(Y,Gd)_2O_3$ ceramic obtained by vacuum sintering at 1850°C for 2 h

8.2.3 Single Crystals

X-ray phosphors can also be single crystalline. The growth of single crystals for special applications is dealt with in Sect. 9.4.

8.3 Materials

8.3.1 X-Ray Phosphors for Conventional Intensifying Screens

The historical role of $CaWO_4$ has already been sketched above. Surprisingly enough, the successful $CaWO_4$ does not satisfy too well the requirements for X-ray phosphors as formulated above. Its X-ray absorption is relatively low, since only one out of the six constituting atoms shows strong X-ray absorption in the range 30–80 keV which is of medical importance, viz. tungsten. Also its density (6.06 g cm^{-3}) is not very high. Its broad band emission (Fig. 8.13) is hard to use completely: a blue-sensitive film

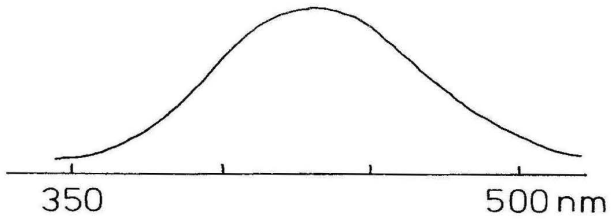

Fig. 8.13. The emission spectrum of $CaWO_4$ under X-ray excitation

does not utilize the green part of the emission. The broadness of this emission band, due to the tungstate group, was discussed in Sect. 3.3.5, and is due to strong coupling with the vibrations. On the other hand, it is an inexpensive and stable material. Most detrimental, however, is the poor X-ray-to-light conversion efficiency of only 6% (see Table 4.5). The maximum efficiency which can be calculated as described in Sect. 4.4 is found to be some 8%, so that there is not much hope of obtaining samples with higher efficiencies than obtained up till now.

Still another problem with $CaWO_4$ is the existence of a severe afterglow (see Sect. 3.4.). X-ray screens with a severe afterglow (or a long persistence) of the emission cause the appearance of a ghost image on a subsequent exposure. The afterglow of $CaWO_4$ can be reduced considerably by adding $NaHSO_4$ to the mixture to be fired. The other drawbacks of $CaWO_4$ are intrinsic, and for this reason, research for better X-ray phosphors has continued.

The first commercial rare-earth X-ray phosphor was $BaFCl:Eu^{2+}$ proposed by the Du Pont company [1]. This material has a higher X-ray absorption and a better conversion efficiency than $CaWO_4$. However, its density is lower (4.56 g. cm^{-3}) and the morphology offers problems (see above).

Figure 8.14 shows the emission spectrum of $BaFCl:Eu^{2+}$. The band maximum is near the sensitivity peak of blue-sensitive film. The emission spectrum at 300 K consists of two parts, viz. sharp-line emission within the $4_f{}^7$ configuration of Eu^{2+} ($^6P_{7/2} \rightarrow {}^8S$), and band emission due to the interconfigurational transition $4f^6 5d \rightarrow 4f^7$. Obviously the lowest level of the $4f^6 5d$ configuration is only slightly higher in energy than the $^6P_{7/2}$ level (see Sect. 3.3.3b).

The emission band of $BaFCl:Eu^{2+}$ is narrower than that of $CaWO_4$ (compare Figs. 8.13 and 8.14). This is due to the fact that the former emission belongs to the indermediate coupling regime, and the latter to the strong coupling regime (see Sect. 3.2). The importance of this difference for the fit to the film sensitivity will be clear.

A better X-ray phosphor with related characteristics is $LaOBr:Tm^{3+}$. This host has the same crystal structure as BaFCl (Fig. 8.9). However, the density of LaOBr is considerably higher: 6.13 g. cm^{-3}. Rabatin has contributed extensive work on phosphors based on this host lattice. It has been described in several patents [1]. Its emission spectrum is given in Fig. 8.15. It consists of intraconfigurational line transitions of Tm^{3+} ($4f^{12}$) in the near ultraviolet and blue spectral region (see Sect. 3.3.2). This phosphor is nowadays a commercial product because of its superb properties.

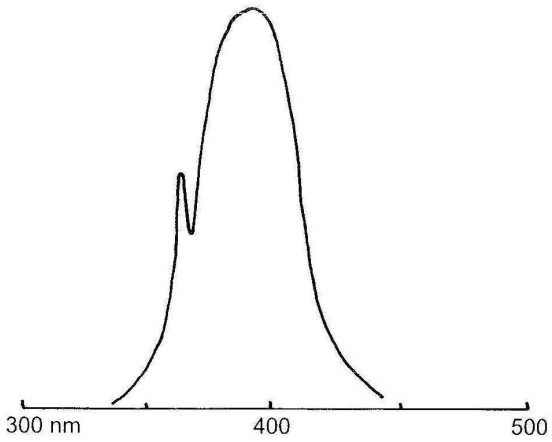

Fig. 8.14. The emission spectrum of $BaFCl:Eu^{2+}$ under X-ray excitation. The peak at shorter wavelengths is due to the $^6P_{7/2} \rightarrow {}^8S$ transition

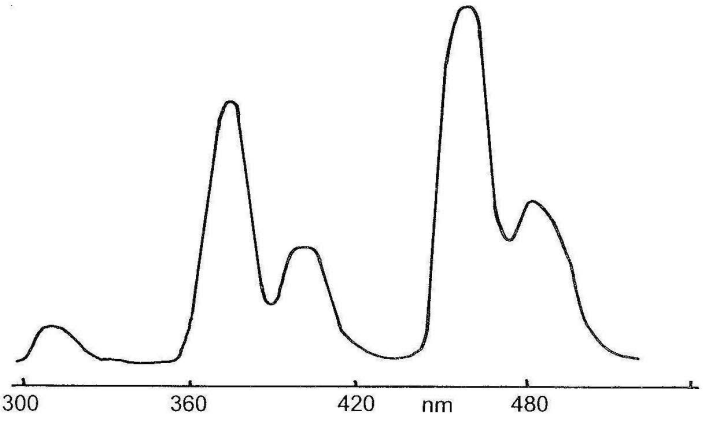

Fig. 8.15. The emission spectrum of $LaOBr:Tm^{3+}$ under X-ray excitation

A green-emitting X-ray phosphor of high quality is $Gd_2O_2S:Tb^{3+}$ described for the first time by Tecotzky [16]. This host also has a layered crystal structure. Using suitable preparation procedures a very nice morphology can be obtained (Fig. 8.10). The density is high, viz. 7,34 g. cm^{-3}, and the X-ray absorption favourable. The conversion efficiency of $Gd_2O_2S:Tb^{3+}$ is about 15%, in good agreement with the maximum efficiency for this host lattice (see Sect. 4.4), and much higher than for $CaWO_4$. The $Gd_2O_2S:Tb^{3+}$ phosphor emits in the green, showing mainly the $^5D_4$–^7F_J line transitions of Tb^{3+} (Sect. 3.3.2). In combination with a green-sensitive film this phosphor acts as a superior X-ray phosphor.

It seemed as if the introduction of $LaOBr:Tm^{3+}$ and $Gd_2O_2S:Tb^{3+}$ indicated the end of the search for new X-ray phosphors. However, this was not the case.

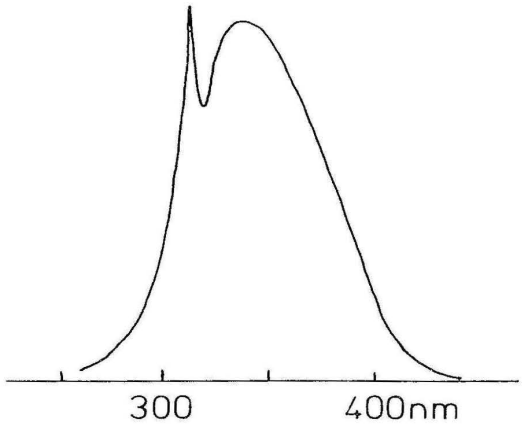

Fig. 8.16. The emission spectrum of M′–$YTaO_4$ under X-ray excitation. The peak at about 312 nm is due to a Gd^{3+} impurity

Later, other very good green-emitting X-ray phosphors were found, for example $GdTaO_4 : Tb^{3+}$, $Gd_2SiO_5 : Tb^{3+}$, and $Gd_3Ga_5O_{12} : Tb^{3+}$. Even more surprising was the invention of the tantalate-based phosphors which are physically similar to $CaWO_4$ [1,17].

The tantalate phosphors are based on M′–$YTaO_4$. This is a modification of $YTaO_4$. The other one is M–$YTaO_4$ [1] which is a distorted variant of scheelite ($CaWO_4$). In the M′ modification of $YTaO_4$ the Ta^{5+} ions are in six coordination. The density is 7.55 g. cm^{-3}. To obtain particles useful for screen production a flux has to be used in the preparation (Li_2SO_4). Figure 8.16 shows the emission spectrum of M′-$YTaO_4$. The band emission is due to a charge-transfer transition in the tantalate group (Sect. 3.3.5). This phosphor is essentially an ultraviolet emitter. The replacement of part of the tantalum by niobium shifts the emission to longer wavelengths (niobate emission). The favourable X-ray absorption of $YTaO_4$ becomes clear from Fig. 8.17. Conversion efficiencies of up to 9% have been obtained. This value is equal to the maximum efficiency to be expected for this compound (see Sect. 4.4).

Even more interesting materials are phosphors based on M′–$LuTaO_4$, which is the densest white material which is not radioactive (d = 9.75 g. cm^{-3}) (1). The X-ray absorption is also higher than for the yttrium analogue (see Fig. 8.17). However, the high price of pure Lu_2O_3 will probably prevent commercial application. In conclusion, the best X-ray phosphors for the conventional X-ray intensifying screen are at the moment $LaOBr : Tm^{3+}$, $Gd_2O_2S : Tb^{3+}$, and M′–$YTaO_4$(: Nb).

8.3.2 X-Ray Phosphors for Photostimulable Storage Screens

The most popular X-ray phosphor for this purpose is undoubtedly $BaFBr : Eu^{2+}$. Its luminescence properties are similar to those of the isomorphous $BaFCl : Eu^{2+}$ (Sect. 8.3.1). As discussed in Sect. 8.1.3 the storage is due to electron trapping by anion vacancies (F-center formation), and hole trapping by a variety of centers (for

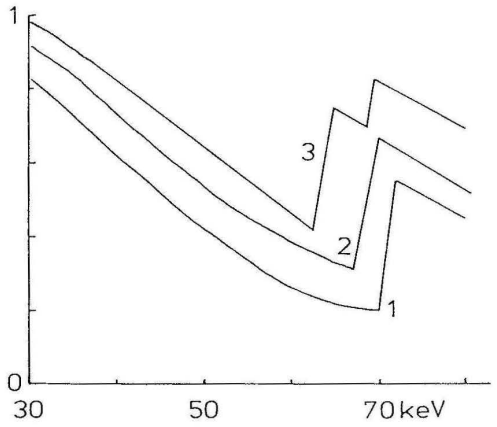

Fig. 8.17. The relative X-ray absorption of (*1*) $CaWO_4$, (*2*) $YTaO_4$ and (*3*) $LuTaO_4$ in the region of the K X-ray absorption edge (cf. Fig. 8.1)

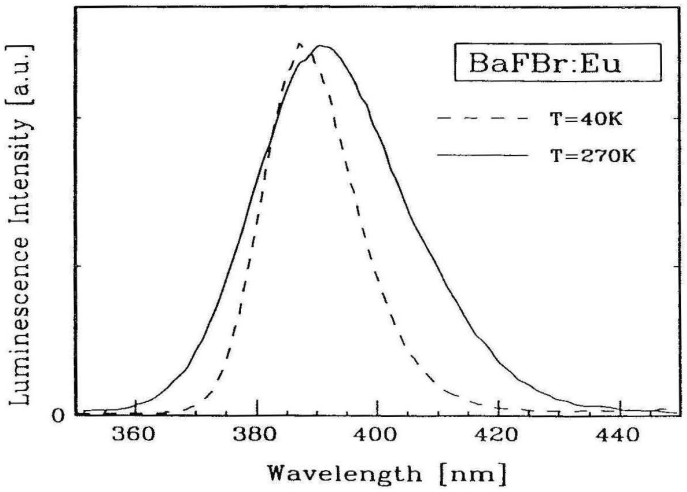

Fig. 8.18. The emission spectrum of $BaFBr:Eu^{2+}$ at 40 and 270 K. After H.H. Rüter, thesis, University Hamburg, 1991

example an oxygen on a fluorine site, or a V_K center (Sect. 3.3.1)). The photostimulable luminescent (PSL) center is thought to consist of three spatially correlated centers, viz. the electron trap, the hole trap and the luminescent center. Figures 8.18 and 8.19 show the emission spectrum and the optical stimulation spectrum of the emission of $BaFBr:Eu^{2+}$. This emission is due to the $4f^6 5d \rightarrow 4f^7$ transition on the Eu^{2+} ion. The stimulation spectrum coincides with the absorption spectrum of the F centre, indicating that the first step in the stimulation is excitation of the trapped electron.

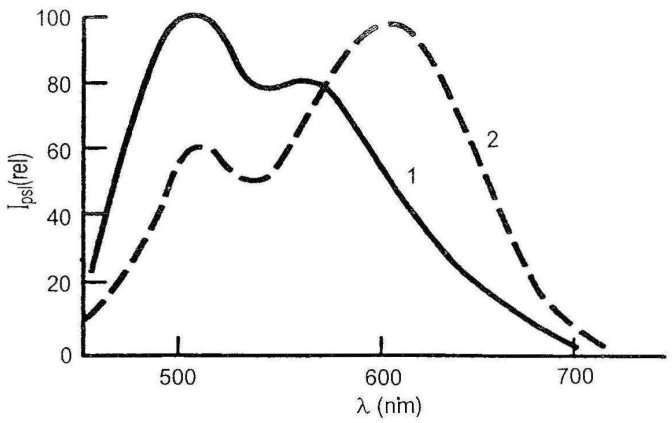

Fig. 8.19. The stimulation spectrum of BaFBr:Eu^{2+} before (*1*) and after (*2*) annealing at 550°C. The intensity of the stimulated emission (I_{psl}) is plotted versus the stimulating wavelength λ

It has been found that only the bromine F centers contribute to the photostimulability, although the X-ray irradiation creates both fluorine and bromine F centres [18]. These authors have also derived estimates of the concentrations of defect centers in a particular $BaFBr:Eu^{2+}$ sample. Even if these values are not very reliable, they illustrate how complicated the physical mechanisms in a storage phosphor may be: 82% of the centers created by irradiation are fluorine F centers or variants thereof; these do not contribute to the photostimulable luminescence. The remaining 18% of the created centers are bromine F centers. Of these about one quarter are spatially correlated to the hole center and the Eu^{2+} ion, i.e. they yield PSL via a tunelling mechanism; the others are not correlated and need thermal activation via the conduction band in order to yield PSL. These estimated concentrations depend strongly on the history of the sample and on the Eu^{2+} concentration.

Another X-ray storage phosphor is $RbBr:Tl^+$. The luminescent center is the Tl^+ ($6s^2$) ion which emits by a $6s6p \rightarrow 6s^2$ transition (Sect. 3.3.7). The electron is trapped at a bromine vacancy, the hole is assumed to be trapped at a Tl^+ ion. The storage state can, therefore, be characterized by $F + Tl^{2+}$. The PSL center consists of these two centers: optical stimulation excites the F center, and the electron recombines with the hole on thallium yielding Tl^+ in the excited state [19]. The efficiency of the photostimulated luminescence of $RbBr:Tl^+$ decreases above 230 K due to a thermal instability of one of the trapped charge carriers.

Some other X-ray storage phosphors are the following:

- $Ba_5SiO_4Br_6:Eu^{2+}$ and $Ba_5GeO_4Br_6:Eu^{2+}$ [20]. Addition of a small amount of niobium improves the storage capacity and changes the storage mechanism [21]. Irradiated samples show the presence of Nb^{4+} (EPR), which is absent before irradiation. This shows that Nb^{5+} on a silicon site acts as an electron trap. Upon optical stimulation the electron becomes available for recombination with the trapped hole, the nature of which is unknown.

These materials can also reach the storage state by ultraviolet excitation. The niobate group absorbs this irradiation in a charge-transfer transition (Sect. 3.3.5). The charge-transfer state is assumed to dissociate: the electron remains at the niobium and the hole leaves the niobate group to be trapped somewhere else. The X-ray and UV excited storage states are identical.

- $Ba_3(PO_4)_2 : Eu^{2+}$. This is an efficient photoluminescent Eu^{2+} phosphor. Upon addition of a small amount of La^{3+} it obtains a large storage capacity [22]. EPR measurements on the storage state show that it contains H^0. It is assumed that the presence of La^{3+} is charge compensated by H^+ ($2Ba^{2+} \rightarrow La^{3+} + H^+$) which is available during the preparation (the phosphate source is $(NH_4)_2HPO_4$). The H^+ ion acts as an electron trap. The EPR signal disappears together with the storage state. The hole is thought to be trapped at the PO_4^{3-} group.
- $Y_2SiO_5 : Ce^{3+}$ [23]. In this material electrons are trapped by oxygen vacancies, and holes by Ce^{3+} (giving Ce^{4+}). Thermal or optical stimulation results in recombination of electron and hole on the Ce^{3+} ion yielding Ce^{3+} emission around 400 nm with a very short decay time (35 ns) (Sect. 3.3.3). The centers are spatially correlated. Codoping with Sm^{3+} changes the storage characteristics, since the electron is now (also) trapped at Sm^{3+} (giving Sm^{2+}). This is shown in Figs. 8.20 and 8.21). Photostimulation occurs by photoionization (Sect. 4.5) of the Sm^{2+} ion.

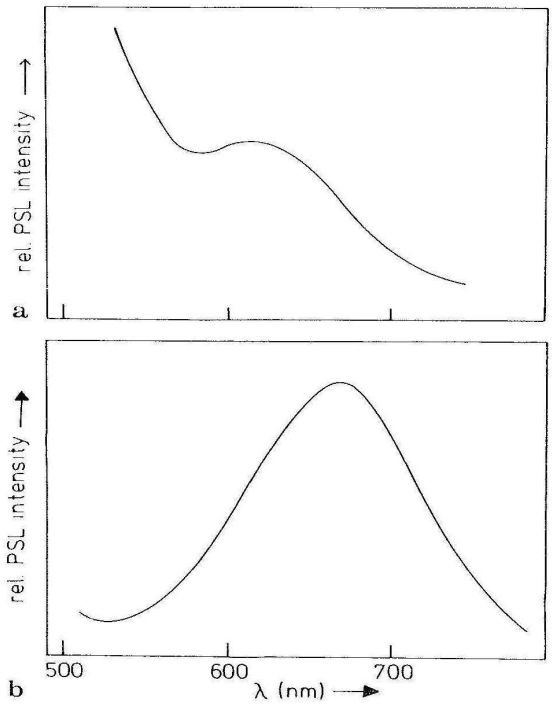

Fig. 8.20. The stimulation spectrum of the Ce^{3+} emission (400 nm) of X-ray irradiated $Y_2SiO_5 : Ce^{3+}$ (*a*) and $Y_2SiO_5 : Ce^{3+}, Sm^{3+}$ (*b*)

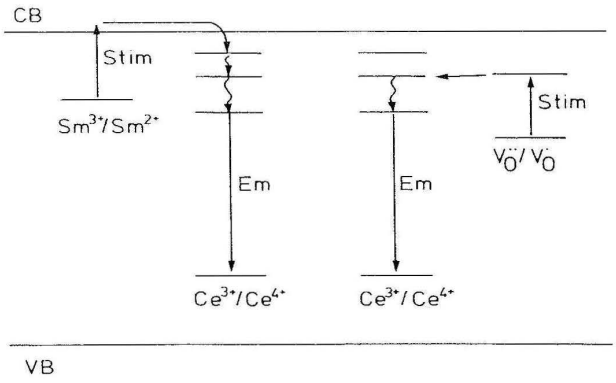

Fig. 8.21. Schematic representation of the model for the recombination in $Y_2SiO_5:Ce^{3+}$ (right) and $Y_2SiO_5:Ce^{3+}$, Sm^{3+} (left). The valence and conduction bands are given by VB and CB, respectively. *Stim* and *Em* stand for stimulation and emission, respectively

These examples show that X-ray storage phosphors have a strongly varying chemical composition which is even wider than the examples suggest. The physical mechanisms of the storage are insufficiently known. Therefore, $BaFBr:Eu^{2+}$ will not be necessarily the phosphor applied in the future.

8.3.3 X-Ray Phosphors for Computed Tomography

A detailed overview of the conventional single crystalline phosphors has been given by Farukhi [24] and Grabmaier [25]. The most important ones are NaI:Tl, CsI:Tl, $CdWO_4$, $ZnWO_4$ and $Bi_4Ge_3O_{12}$.

NaI:Tl is eliminated because of serious afterglow problems, its hygroscopic behavior and its emission maximum in the blue range (415 nm) (see also Sect. 9.5.1). $ZnWO_4$ and $Bi_4Ge_3O_{12}$ have a too low light output for X-ray CT application (20% and 10% of CsI:Tl, respectively) (see also Sects. 9.5.2 and 9.5.3). The two remaining phosphors, CsI:Tl and $CdWO_4$, have several drawbacks, as seen in Table 8.1. CsI:Tl shows an excessive afterglow which cannot be influenced by growth techniques or by codoping, and its light output depends on its irradiation history. This is known as hysteresis and varies for different crystal ingots. The remaining crystal $CdWO_4$ exhibits a low afterglow, a short decay time and a sufficiently high light output (see also Sect. 9.5.2). However, the material is toxic, very brittle and has the tendency to crack parallel to its cleavage plane during machining.

A new class of phosphors based on ceramic materials has been introduced by several groups [26,27]. These materials are derivatives of the well-known rare-earth phosphor systems of oxides and oxysulfides. The most promising ceramic host lattices are $(Y,Gd)_2O_3$, Gd_2O_2S and $Gd_3Ga_5O_{12}$.

The reader will recognize these from earlier paragraphs: $Y_2O_3:Eu^{3+}$ as a lamp phosphor (Sect. 6.4.1.4) and a projection-television phosphor (Sect. 7.3.4),

Table 8.1. Characteristic data of potential phosphors for CT detectors.

	CsI : Tl	$CdWO_4$	$(Y,Gd)_2O_3$: Eu, Pr	Gd_2O_2S : Pr, Ce	$Gd_3Ga_5O_{12}$: Cr, Ce
Type	Single crystal	Single crystal	Ceramic	Ceramic	Ceramic
Structure	Cubic	Monoclinic	Cubic	Hexagonal	Cubic
Density (g cm^{-3})	4.52	7.99	5.91	7.34	7.09
Attenuation coefficient 150 keV (cm^{-1})	3.21	7.93	3.40	6.86	4.36
Emission maximum (nm)	550	480	610	510	730
Light output 80 keV (rel.)	100	30	~ 67	~ 75	~ 60
Decay time (μs)	0.98	8.9	~ 1000	~ 3	140
Afterglow % after 3 ms	2	< 0.1	~ 3	$\lesssim$ 0.1	$\lesssim$ 0.1
Afterglow % after 50 ms	0.2	0.005	0.005	0.005	~ 0.01
Optical quality	Clear	Clear	Trans-parent	Trans-parent	Trans-parent
Chemical stability (attacked by)	Water	HCl	Conc. HCl	HCl	Conc. HCl
Mechanical behavior (20°C)	Plastic Defor-mable	Brittle Cleavable	Brittle High strength	Brittle High strength	Brittle High strength

$Y_2O_2S:Eu^{3+}$ as a cathode-ray phosphor (Sect. 7.3.3) and $Gd_2O_2S:Tb^{3+}$ as an X-ray phosphor for intensifying screens (Sect. 8.3.1), and the garnets $Y_3Al_5O_{12}:Ce^{3+}$ and $(Y,Gd)_3(Al,Ga)_5O_{12}:Tb^{3+}$ as a phosphor in special deluxe lamps (Sect. 6.4.1.7) and as phosphors for projection television tubes (Sect. 7.3.4) and X-ray intensifying screens (Sect. 8.3.1), respectively.

For C.T. an efficient activator for $(Y,Gd)_2O_3$ is the Eu^{3+} ion with its characteristic $^5D_0$–^7F_J emission (Sect. 3.3.2); its decay time is actually too long for this application. In Gd_2O_2S the Pr^{3+} ion is used as an activator with mainly $^3P_0 \rightarrow {}^3H_J$, ^3F_J emission and a decay time of 3 μs. In $Gd_3Ga_5O_{12}$ the Cr^{3+} ion is used. It yields broad-band (infra)red emission due to the $^4T_2 \rightarrow {}^4A_2$ crystal-field transition (Sect. 3.3.4). This emission occurs because the crystal field at the Cr^{3+} ion in $Gd_3Ga_5O_{12}$ is relatively weak. Due to the parity selection rule (Sect. 2.1) the decay time is relatively long (140 μs). The luminescence properties of ceramic scintillators do not differ significantly from those of the related crystal or powder samples, but deviations occur in the light output depending on the different optical behaviour of ceramics.

The afterglow (Sect. 3.4), which is strongly dependent on the defect concentration in the host lattice, can be lowered by special codopants. Such an efficient codopant is praseodymium in $(Y,Gd)_2O_3:Eu^{3+}$, and cerium in $Gd_2O_2S:Pr^{3+}$ as well as in $Gd_3Ga_5O_{12}:Cr$. However, it should be realized that a decrease of the afterglow level

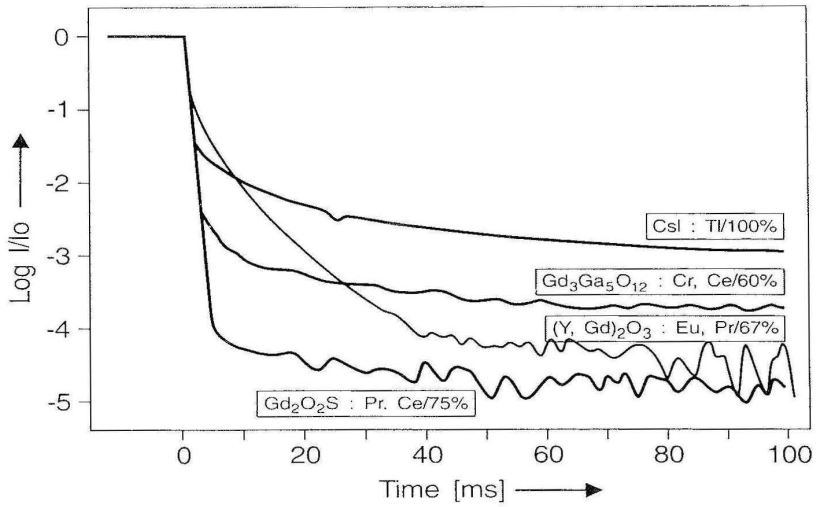

Fig. 8.22. Afterglow behavior of various scintillators for X-ray CT excitation with respect to their light output

by codoping is always correlated with a decrease of the light output. Models which try to explain how the codopants lower the afterglow level can be found in refs [28] and [29]. In summary, Fig. 8.22 shows the afterglow behaviour of various scintillators with respect to their light output, and Table 8.1 shows the properties of some ceramic phosphors compared to the single crystals CsI : Tl and $CdWO_4$.

8.4 Outlook

The search for new X-ray phosphors for conventional X-ray intensifying screens is reaching its end. A number of satisfactory materials are available, and efficiencies cannot be expected to become much higher. For specialized applications there may be some need for improvement.

Less satisfactory, but more challenging is the situation of the X-ray storage phosphors. A good material is available, viz. $BaFBr : Eu^{2+}$. However, the physics of the storage mechanism is incompletely understood. It is not known whether the present efficiencies are close to the theoretical limits or not. Also the development of potential applications has only just started. Therefore we may expect new results in this area in the coming years.

Computed tomography has shown considerable improvements for a couple of years. For the future the introduction of ceramic plates may be expected. Also here the introduction of new materials cannot be excluded, but seems less probable.

References

1. Brixner LH (1987) Mat. Chem. Phys. 16:253
2. Sonoda M, Takano M, Migahara J, Shibahara Y (1983) Radiology 148:833
3. McKeever SWS (1985) Thermoluminescence of solids. Cambridge University Press, Cambridge
4. Takahashi K, Miyahara J, Shibahara Y (1985) J. Electrochem. Soc. 132:1492; Iwabuchi Y, Mori N, Takahasji K, Matsuda T, Shionoya S (1994) Jap. J. Appl. Phys., 33:178
5. Meijerink A, Blasse G (1991) J. Phys. D: Appl. Physics 24:626
6. Rtter HH, von Seggern H, Reiniger R, Saile V (1990) Phys. Rev. Letters 65:2438
7. Koschnick FK, Spaeth JM, Eachus RS, McDugle WG, Nuttal RHD (1991) Phys. Rev. Letters 67:3751
8. von Seggern H (1992) Nucl. Instrum. Methods A 322:467
9. Hounsfield GN (1973) Brit. J. Radiol. 46:1016
10. Alexander J, Krumme HJ (1988) Electromedica 56:50
11. Rossner W, Grabmaier BC (1991) J. Luminescence 48,49:29
12. Kingery WD, Bowen HK, Uhlmann DR (1975) Introduction to Ceramics. Wiley, New York
13. Engineered Materials Handbook (1992) Vol. 4 Ceramics and Glasses ASM International
14. Gassner W, Rossner W, Tomande G (1991) In: Vincencini P (ed) Ceramic today-tomorrow's ceramics. Elsevier, Amsterdam, p 951
15. Grabmaier BC, Rossner W, Leppert J (1992) Phys. Stat. Sol. (a) 130: K 183
16. Tecotzky M (1968) Electrochem. Soc. Meeting, Boston, May
17. Brixner LH, Chen Hy (1983) J. Electrochem. Soc. 130:2435
18. Thoms M, von Seggern H, Winnacker A (1991) Phys. Rev. B 44:9240
19. von Seggern H, Meijerink A, Voigt T, Winnacker A (1989) J. Appl. Phys. 66:4418
20. Meijerink A, Blasse G, Struye L (1989) Mater. Chem. Phys. 21:261; Meijerink A, Blasse G (1991) J. Phys. D: Appl. Phys. 24:626
21. Schipper WJ, Leblans P, Blasse G, Chem. Mater., in press; Schipper WJ (1993) thesis, University Utrecht
22. Schipper WJ, Hamelink JJ, Langeveld EM, Blasse G (1993) J. Phys. D: Appl. Phys. 26:1487
23. Meijerink A, Schipper WJ, Blasse G (1991) J. Phys. D: Appl. Phys. 24:997
24. Farukhi MR (1982) IEEE Trans. Nucl. Sci., NS-29:1237
25. Grabmaier BC (1984) IEEE Trans. Nucl. Sci., NS-31:372
26. Greskovich CD, Cusano DA, Di Bianca FA (1986) US Pat. 4,571,312; Greskovich CD, Cusano DA, Hoffman D, Riedner RJ (1992) Am. Ceram. Soc. Bull. 71:1120
27. Yokota K, Matsuda N, Tamatani M (1988) J. Electrochem. Soc. 135:389
28. Blasse G, Grabmaier BC, Ostertag M (1993) J. Alloys Compounds 200:17
29. Grabmaier BC (1993) Proc. of the XII int. conf. defects in insulating materials. World Scientific, Singapore p 350

CHAPTER 9

X-Ray Phosphors and Scintillators (Counting Techniques)

9.1 Introduction

In Chapter 8, the excitation was exclusively by X-ray irradiation. In this chapter the stress will be on other types of ionising radiation such as γ rays and charged particles. In many cases, their energy will be higher than that of X rays. In all applications the counting of the number of ionizing events is essential. This method of radiation detection gives information on quantities such as the kind of radiation, the intensity, the energy, the time of emission, the direction and the position of the emission. Many of the applications use luminescent materials in the form of large single crystals.

The organisation of this chapter is as follows. In Sect. 9.2 the principles of the interaction between ionizing radiation and condensed matter will be dealt with. In Sect. 9.3 the principles of several applications will be discussed and the material requirements specified. The preparation of the materials will concentrate on single crystal growth and will be discussed in Sect.9.4. Finally Sect. 9.5 will give a survey of the several materials in use and Sect. 9.6 will present a future outlook. For more details than presented here, the reader is referred to the proceedings of a recent workshop [1].

9.2 The Interaction of Ionizing Radiation with Condensed Matter

There are three ways in which ionizing (electromagnetic) radiation interacts with matter, viz.

- the photoelectric effect
- the Compton effect
- pair production.

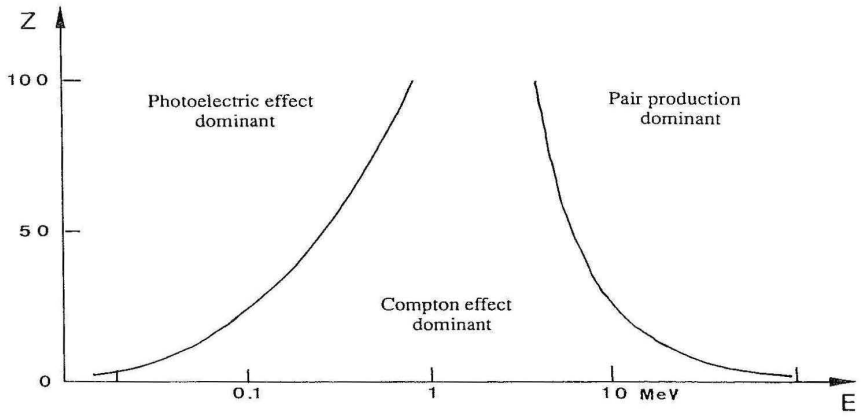

Fig. 9.1. The relative importance of the three major types of interaction of γ-rays with condensed matter. The atomic number Z is plotted linearly versus the γ-ray energy E which is plotted logarithmically (in MeV)

In the photoelectric effect, the photon is absorbed by an ion and subsequently a (photo)electron is ejected from one of the shells, usually the K shell. The photoelectron acquires an energy E_{pe} which is equal to the difference between the photon energy $h\nu$ and the binding energy E_b of the electron. This energy E_b appears in the form of X rays or Auger electrons when the vacancy in the K-shell is filled. The X rays are absorbed in a second photoelectric process and the complete energy of the incident photon is absorbed in the scintillator.

In the Compton effect, the photon interacts with an electron of an ion in the solid and transfers part of its energy to this electron. The result is a Compton scattered photon with energy $h\nu'$ ($\nu' < \nu$) and a so-called Compton electron with energy E_c. The scattered photon may leave the scintillator or may interact with the scintillator (but at a site different from the first interaction). In the latter case the incident photon gives two light centers at different sites which makes the Compton effect undesirable for position-sensitive detection. If the scattered photon leaves the scintillator crystal, less luminescent radiation is produced than in the case of the photoelectric effect.

For photons with very high energy the process of pair production results: the photon is completely absorbed and converted into an electron-positron pair. The positron is annihilated with another electron with the emission of two photons of 0.511 MeV.

The relative importance of the three above-mentioned interaction mechanisms depends on the energy of the incident photon and on the atomic number of the absorbing ions in the scintillator. This is illustrated in Fig. 9.1.

Charged particles such as electrons, muons, or α particles lose energy through Coulomb interaction with the electrons in the solid. Two categories can be defined:

- weakly penetrating particles (low-energy electrons, protons, α particles); the rate of energy loss increases as the charge and the mass of the particle increases, whereas the scintillation yield decreases: for equal energies, a proton produces $\frac{1}{4}$

to $\frac{1}{2}$ the light of that of an electron, whereas α particles produce only $\frac{1}{10}$ of this light.
- minimum ionizing particles; they are singly charged and have low mass and high energy (fast electrons, cosmic muons). Their energy loss per unit pathlength is small.

9.3 Applications of Scintillator Crystals

Scintillator crystals are used in medical diagnostics, in industrial applications and in scientific applications [1]. A spectacular application in the latter field is the use of scintillator crystals in electromagnetic calorimeters [1,2]. These are used in high-energy physics, nuclear physics and astrophysics to count electrons and photons. The largest calorimeter was built at CERN (Geneva) in the late 1980s. It contains 12 000 $Bi_4Ge_3O_{12}$ (see Sects. 3.3 and 5.3) crystals of 24 cm in length, representing a total volume of 1.2 m^3 [2].

The energy of the radiation or the particles involved in the latter application are very high ($\sim$ GeV). As a consequence the conversion efficiency of the scintillator can be low. This efficiency is, in this field, expressed differently from the definitions given in Sect. 4.3, viz. as light yield expressed in photons per MeV. In view of the large amounts of energy collected in the calorimeter, a light yield of only 200 photons per MeV suffices. The reader should note that for emitted photons of, for example, 4 eV, this corresponds to a radiant or energy efficiency (Sect. 4.3) of 0.08%. Maximum efficiencies, estimated in Sect. 4.4, are of the order of 10–20%. It is exceptional that such a low efficiency suffices for an application.

However, in almost all other cases, a high light yield is important. The accuracy of the observation is higher if the number of observed photons, N, is larger. Energy and time resolution are proportional to $\frac{1}{\sqrt{N}}$. The basic principle of scintillation counting is that the light output of the scintillator is proportional to the energy of the incident photon [3]. In order to detect these photons, the scintillator is coupled to a photomultiplier tube in which the photons are converted into photoelectrons which are multiplied and give a pulse with an amplitude proportional to the number of photons. For a linear detector response all components should also have a linear response.

A γ-ray spectrometer should be able to discriminate between γ-rays with slightly different energy. This quality is characterized by the so-called energy resolution which depends on the light yield as indicated above.

The time resolution is defined as the ability to give accurately the moment of absorption of the photon in the scintillator. The time resolution is proportional to $\frac{1}{\sqrt{N}}$ and the decay time τ (Sect. 5.3.1). It is obvious that the moment of the absorption event is found most accurately if τ is short.

Scintillators also play an important role in medical diagnostics [4]. X-ray imaging has already been dealt with in Chapter 8. In this chapter we will mention the γ-ray camera. Radioisotopes are introduced into the body, usually in the form of chemical compounds labeled with a suitable radioactive element. A commonly used one is ^{99m}Tc

Table 9.1. Some commonly used radionuclides

Radionuclide	half life*	E_γ(keV)
^{99m}Tc	6.02 h	140.5
^{81m}Kr	13.3 s	190.7
^{123}I	13.0 h	158.9
^{67}Ga	3.26 d	93.3; 184.6; 300.3

* h: hour; s: second; d: day

Table 9.2. Some important radio isotopes in positron imaging and some examples of their application [5]

Isotope	$T_{1/2}$ (min.)	E_{β^+} max. (MeV)	labeled substance	example of use
^{11}C	20.4	0.961	^{11}C-glucose	brain metabolism
			^{11}C-putrescine	tumor metabolism
^{13}N	9.96	1.19	$^{13}NH_3$	heart blood flow
^{15}O	2.04	1.73	$^{15}O_2$	oxygen consumption
^{124}I	4.2 days	2.13	$^{124}I^-$	thyroid studies
		1.53		

(see also Table 9.1). By measuring the radiation outside the body, a functional image can be obtained (note that the methods described in Chapter 8 were non-invasive). This emitted radiation (120–150 keV) is measured by a γ-ray camera which usually contains a scintillator crystal. Common γ-ray cameras yield a two-dimensional image of the radioactivity distribution. When the camera is rotated around the patient and/or two opposed γ-ray cameras are used, it is possible to construct a three-dimensional image (compare computed tomography, Sect. 8.1.4). This technique is called SPECT (single-photon emission computed tomography). This method does not allow to make accurate corrections for radiation attenuation in the body. Therefore, SPECT does not produce very good images, especially not of deeper-lying organs.

A different method is PET (positron emission tomography) [4,5]. It is also an in-vivo tracer technique, but uses the annihilation of positrons. Actually, one is confined to positron emitters for in-vivo studies of the distribution of elements in biologically active compounds, viz. carbon, nitrogen, oxygen. Metabolic processes can be studied in this way (see also Table 9.2).

The emitted positron cannot penetrate far into tissue; its range is only a few millimeters. After slowing down, it is annihilated with an electron. In most cases two photons (γ radiation) are emitted with an energy of 511 keV each under 180°. PET exploits the collinear emission by putting a coincidence requirement on detectors opposed to each other: an event detected simultaneously in the two detectors implies that the annihilation took place somewhere along the line between the two points of detection (Fig. 9.2). From the coincidence data, images are constructed which present the three-dimensional distribution of the radioactivity. The images are corrected for

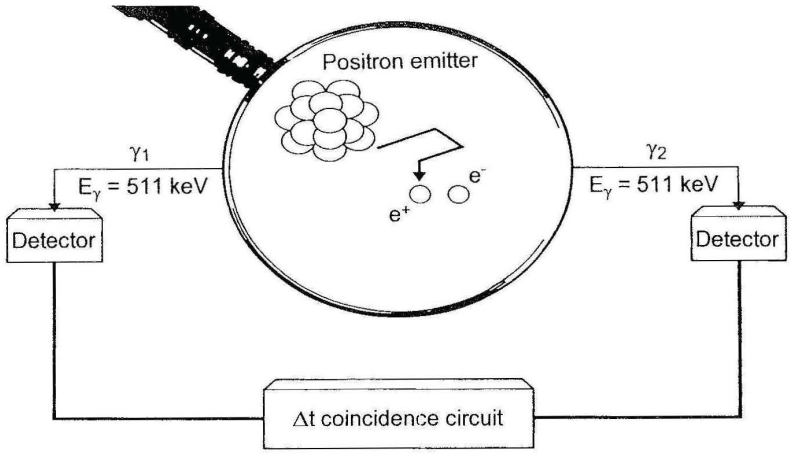

Fig. 9.2. The principle of positron emission tomography. Under the magnifying glass the positron emission has been drawn. See also text

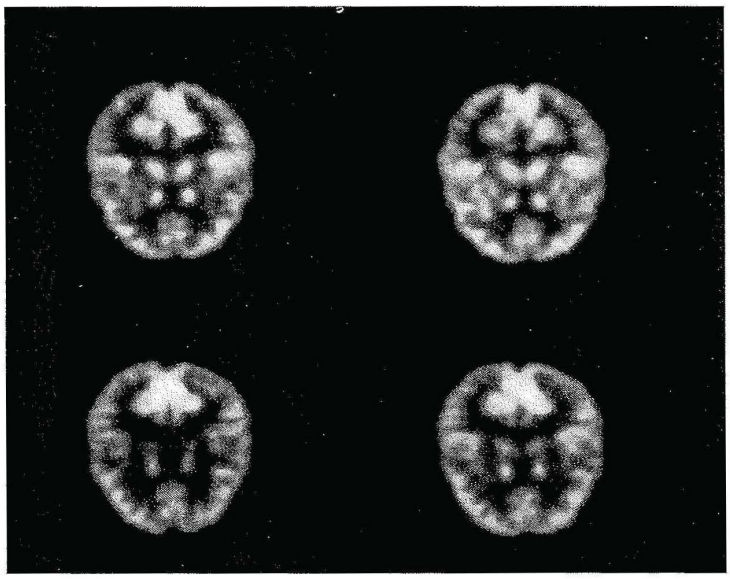

Fig. 9.3. An image of several heads obtained by positron emission tomography

radiation attenuation in the body which is not possible with SPECT. An example of a PET scan is shown in Fig. 9.3.

As mentioned above, the scintillation light can be detected using a photomultiplyer. There are also other possibilities. Among the solid-state photon detectors, silicon photodiodes have become popular. These were mentioned previously (Sect. 8.1.4,

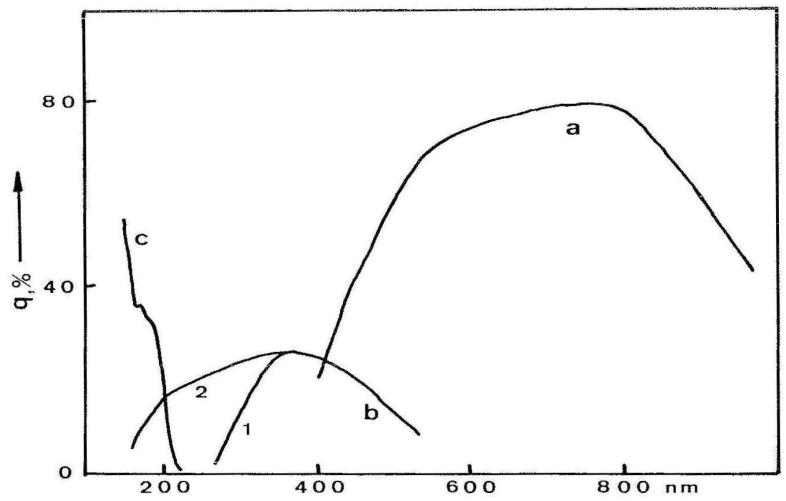

Fig. 9.4. The quantum efficiencies q(%) of the more important radiation detectors. (*a*): silicon photodiode; (*b*): photomultiplyer tube with glass (*1*) and with quartz (*2*); (*c*) solid scintillator proportional counter with gas-filled detector

computed tomography). Their sensitivity reaches a maximum for wavelengths longer than 500 nm.

A different detection unit is the solid-scintillator proportional counter [6]. It consists of a scintillator with ultraviolet emission in a multiwire chamber filled with an organic vapor. The organic molecules are ionized by the ultraviolet photons and the resulting photoelectrons are detected in the multiwire chamber. A popular molecule in this aspect is TMAE (tetrakis (dimethylamino) ethylene). Figure 9.4 presents the spectral sensitivities of the detectors mentioned.

Industrial applications form a very broad field in which imaging as well as counting techniques are applied. We can mention X-ray tomography, oil well logging, process control, security systems, container inspection, mineral processing and coal analysis [7].

Table 9.3 gives a survey of the scintillator requirements in the various applications [8,9]. As a matter of fact the atomic number of the constituents as well as the density should be high. An exception to this are scintillators for neutron detection; they should contain Li, B or Gd. Further, scintillator materials should be rugged and radiation hard. Of course they should not be hygroscopic. The emission range is, among other factors, dictated by the detector used. The light yield should be high; only in the large calorimeters used in high-energy physics in the large colliders is this requirement not essential.

Maximum possible light yields can be predicted from the maximum possible efficiency (Sect. 4.4). Some examples are given in Table 9.4 [10]. As a matter of fact the quantum efficiency of the luminescent center should be high, and competing (quenching) centers should be absent (Sect. 4.4, Refs [10,11]).

Table 9.3. Scintillator requirements in various applications (after Ref. [8])

Application	Light yield (photons/MeV)	decay time (ns)	emission (nm)
counting techniques			
Calorimeter (high energy physics)	> 200	< 20	> 450
Calorimeter (low energy physics, nuclear physics)	hign	varies	> 300
Positron emission tomography (PET)	high	< 1	> 300*
γ-ray camera	high	less imperative	> 300
industrial applications	high	varies	> 300
integrating techniques			
computed tomography (CT)	high	no afterglow	> 500
X-ray imaging	high	less imperative	> 350

* but < 250 nm when using a multiwire chamber

Table 9.4. Light yields of some scintillators in relation to their maximum efficiency [10]. See also text

Scintillator	light yield (ph/MeV)	η from light yield (%)	η_{max} (Sect. 4.4)
NaI : Tl	40.000	12	19
Lu_2SiO_5 : Ce	25.000	8	10
$Bi_4Ge_3O_{12}$	9.000	2	2*

* after correction for thermal quenching

Short decay times can be obtained by using luminescent ions with allowed emission transitions. In the field of inorganic materials the best examples are the $5d \rightarrow 4f$ transitions ($\tau \sim 10$ ns) (Sects. 2.3.4 and 3.3.3) and the cross luminescence ($\tau \sim 1$ ns) (Sect. 3.3.10) [11]). The afterglow is governed by the presence of traps in the host lattice as described in Sect. 3.4.

One of the most important applications of thermoluminescence (Sect. 3.5) is in the field of radiation dosimetry [12,13]. Here a material is exposed for a specific time to a radiation field. The absorbed doses ranging from 10^{-2}mGy to 10^5Gy (1Gy (1 gray) = 100 rd (rad); 1 rad is equivalent to an absorbed energy of 0.01 J/kg) are measured by monitoring the thermoluminescence after the exposure time. Many materials display an intensity of thermoluminescence which is proportional to the amount of radiation absorbed. This led Daniels and colleagues in the early 1950s to use thermoluminescence as a means of radiation dosimetry.

The first application was in 1953 when LiF was used to measure the radiation following an atomic weapon test [12]. Later this material was used in hospital to

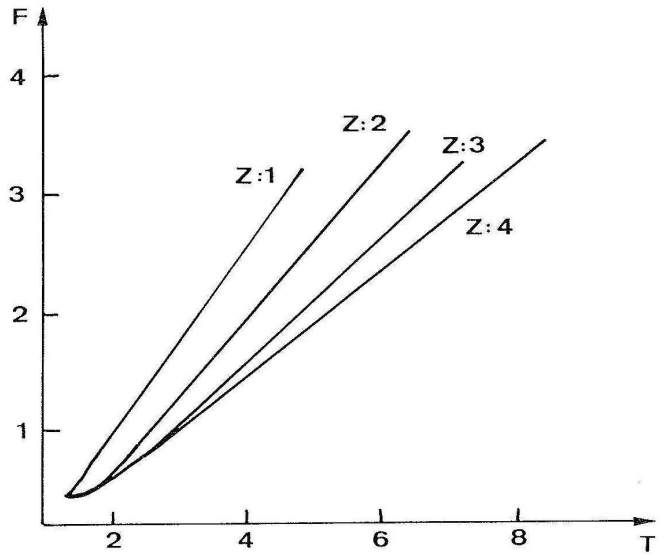

Fig. 9.5. The identification of particles in a fast component (F) vs total (T) intensity plot (BaF_2)

measure internal radiation doses received by cancer patients treated with radionuclides. Following this pioneering work, an enormous amount of work has been performed in order to extend this application. Many materials have been found (for a survey, see Ref. [12]). For example, LiF was optimized by doping with 170 mol ppm Mg and 10 mol ppm Ti.

For a further study of this application which has rather complicated aspects we refer to Ref. 12. In that book the reader will also find other applications of thermoluminescence, e.g. age determination.

Finally we mention the possibility of particle identification by using a scintillator crystal. This method makes use of the fact that certain scintillators, for example BaF_2 and $CsI:Tl^+$, show two different emissions, one with a shorter and one with a longer decay time (see Sect. 9.5). Wisshak et al. were able to discriminate γ photons and charged hadrons using a BaF_2 scintillator [14]. A more general example, also using BaF_2, has been given by Migneco et al. [15].

The intensity ratio of the fast and the total emissions depends on the nature of the particle. This is shown in Fig. 9.5 where the fast light output is plotted vs the total light output for a BaF_2 scintillator. The contribution of the fast component decreases in the sequence γ-rays and cosmic muons, protons, deuterons, tritons and α particles. The penetration depth decreases in the same sequence, i.e. the excitation density increases. The consequence of this will be discussed in the paragraph on BaF_2 (Sect. 9.5.7).

9.4 Material Preparation (Crystal Growth)

Scintillators which are used for the detection of strongly ionizing radiation, as discussed in this chapter, are practically always applied as single crystals. The reason for this is that the scintillator should have a high optical transmission in the emission region, so that the emission can escape efficiently. This sometimes requires very large crystals without gas bubbles or precipitates, since these would result in light scattering. It is probable that certain imperfections in the crystal will also be detrimental for radiation hardness. When dopants have to be used, for example Tl^+ in NaI, the dopant will never have a uniform distribution over the whole crystal volume.

All commercially available scintillator crystals are grown from the melt. But crystals can only be grown from the melt if the compound from which a single crystal is desired has a congruent melting point, does not decompose before melting, and has no phase transition between the melting point and room temperature.

Two of the frequently applied melt growth methods are shortly discussed, viz. the Bridgman-Stockbarger method and the Czochralski method. In the Bridgman-Stockbarger technique both crystal and melt are confined within a solid container such that the three-phase boundary is between crystal, melt and container material. This technique can be divided into those in which a crystal-melt interface is propagated vertically or horizontally, those in which the whole charge is melted initially and subsequently crystallized progressively, and those in which a molten zone is established and traversed along an ingot.

Figure 9.6 shows a schematic view of the vertical directional solidification. The resistance-heated furnace is composed of several separate heating zones (in Fig. 9.6 only two zones are shown), the temperature of which can be programmed and controlled separately. The cylindrical ampoules containing the charge are supported or the furnace can be lowered during the crystal growth process.

With this methods growth rates of about one millimeter per hour can be maintained. Alkali halide crystals ranging up to 30 inches ($\approx$ 75 cm) in diameter and half a ton of mass can be grown. Such crystals are not truly single, but rather contain five to ten components as delineated by small-angle grain boundaries which crop out at the surface or are evident under strong illumination due to scattering by impurities on the boundaries [16].

If Tl^+-activated alkali halides are desired, thallium iodide has to be mixed with the starting material (NaI or CsI) and dissolved in the melt. The distribution coefficient of thallium in the alkali halide was measured to be about 0.2 for NaI [16] and 0.1 for CsI [17], using the ratio Tl^+ concentration in the crystal/Tl^+ concentration in the melt. During crystal growth the concentration of thallium in the melt will increase, but since thallium is volatile at the melting point of NaI (T_m: 652°C) and CsI (T_m: 623°C), some of the thallium may be lost by evaporation. This means that the Tl^+ concentration in a given crystal will not be constant over the crystal volume. Fortunately the luminescence intensity is nearly constant for Tl^+ concentrations in NaI between 0.02 –0.2 mol per cent [16] and in CsI between 0.06–0.3 mol per cent